Check for updates

Angewandte Chemie International Edition

Angewandte International Edition Chemie

How to cite: *Angew. Chem. Int. Ed.* **2026**, 65, e9878440
doi.org/10.1002/anie.9878440

RESEARCH ARTICLE

Spin-State Engineering of Ni Centers by Dual-Ligand Competitive Coordination for Superior Oxygen Evolution Reaction

Zhiyang Huang[1,2] | Bin Wu[3] | Shifan Zhang[1] | Changtai Xu[1] | Yan Hu[4] | Lixia Wang[5] | Baofa Liu[1] | Biao Fu[1] | Xiaofeng Shi[6] | Mingcheng Gao[1] | Aling Zhou[1] | Xiulin Yang[1] | Tierui Zhang[7] | Lifang Jiao[2]

[1]Guangxi Key Laboratory of Low Carbon Energy Materials, School of Chemistry and Pharmaceutical Sciences, Guangxi Normal University, Guilin, China | [2]Key Laboratory of Advanced Energy Materials Chemistry, Ministry of Education State Key Laboratory of Advanced Chemical Power Sources Collaborative Innovation Center of Chemical Science and Engineering, Nankai University, Tianjin, China | [3]School of Materials Science and Engineering, Nanyang Technological University, Singapore, Singapore | [4]Department of Mechanical and Energy Engineering, Southern University of Science and Technology, Shenzhen, China | [5]Shenzhen Key Laboratory of Micro/Nano-Porous Functional Materials (SKLPM) and Department of Chemistry, Southern University of Science and Technology, Shenzhen, China | [6]School of Environment and Safety Engineering, North University of China, Taiyuan, China | [7]Key Laboratory of Photochemical Conversion and Optoelectronic Materials, Technical Institute of Physics and Chemistry, Chinese Academy of Sciences, Beijing, China

Correspondence: Bin Wu (bin.wu@ntu.edu.sg) | Xiaofeng Shi (xiaofeng_shi1987@163.com) | Xiulin Yang (xlyang@gxnu.edu.cn) | Lifang Jiao (jiaolf@nankai.edu.cn)

Received: 6 January 2026 | **Revised:** 18 March 2026 | **Accepted:** 1 April 2026

Keywords: anion exchange membrane water electrolyzer | dual-ligand competition | oxygen evolution reaction | solar-to-hydrogen efficiency | spin-state modulation

ABSTRACT

Modulating electronic spin states of metal active centers is an effective strategy to address the sluggish oxygen evolution reaction (OER) kinetics. Herein, we utilize a dual-ligand competitive coordination strategy to induce lattice expansion, generate abundant oxygen vacancies and unsaturated coordination sites, and restructure the NiO_6 octahedron. This triggers a pivotal transition of Ni from intermediate-spin (Ni^{2+}) to high-spin (Ni^{3+}) states, which enhances adsorption of OH^- and oxygen-containing intermediates, but also tailors the interfacial microenvironment by enriching free water, thus accelerating OER kinetics. In situ x-ray adsorption spectroscopy further verifies the accelerated adsorption and transformation of oxygen intermediates enabled by this spin reconfiguration. Consequently, the optimized nickel-thiophene-2,5-dicarboxylic $acid_{0.6}$-1,4-$dicarboxybenzene_{0.4}$ dual-ligand metal-organic framework catalyst (marked as Ni-$TDC_{0.6}BDC_{0.4}$) delivers excellent OER performance (230 mV@10 mA cm^{-2}). Using Ni-$TDC_{0.6}BDC_{0.4}$ as the anode, the assembled anion exchange membrane water electrolyzer achieves a low cell voltage of 2.40 V at 1.5 A cm^{-2} and maintains stability for 500 h at 300 mA cm^{-2}. Its photovoltaic-integrated overall water splitting device also attains a 13.23% solar-to-hydrogen efficiency with robust stability. This work provides an innovative synthesis pathway for designing high-performance OER electrocatalysts by tailoring electron spin states.

Zhiyang Huang, Bin Wu, and Shifan Zhang contributed equally to this work.

© 2026 Wiley-VCH GmbH

1 | Introduction

Hydrogen has emerged as an ideal alternative to traditional fossil fuels due to its high energy density and environmental benignity [1, 2]. Electrochemical water splitting, capable of direct utilization of renewable energy sources, is regarded as the core pathway for achieving large-scale green hydrogen production [3, 4]. However, the alkaline oxygen evolution reaction (OER), serving as the anodic half-reaction of water splitting, involves intricate steps (e.g., four-electron transfer and O—H bond cleavage), leading to sluggish reaction kinetics that constitutes the primary bottleneck limiting overall hydrogen production efficiency [5, 6]. As a pivotal implementation of alkaline water electrolysis technology, the anion exchange membrane water electrolyzer (AEMWE) integrates prominent advantages such as relatively high stability, low cost, and excellent safety, thereby playing an indispensable role in sustainable hydrogen production [7]. Nevertheless, the noble metal OER catalysts (such as RuO_2 and IrO_2) commonly used in existing AEMWE systems are plagued by inherent limitations including scarce reserves, high costs, and inadequate long-term stability [8, 9]. Therefore, developing highly efficient, stable, and low-cost non-noble metal OER catalysts is pivotal for advancing AEMWE industrialization.

The rate-determining step (RDS) of OER typically involves the adsorption or desorption of oxygenated intermediates on the active sites. Therefore, optimizing the hybridization strength between the 3d orbitals of transition-metal active centers and the 2p orbitals of oxygen intermediates is crucial for accelerating OER kinetics [10, 11]. This is primarily due to the close correlation between the d-orbital electronic states of the metal centers and the catalytic activity of OER. Notably, spin-state regulation serves as an effective strategy for precise modulation of the electronic configuration [12]. For transition-metal-based OER catalysts (such as Ni, Co, and Fe), the spin state of the metal active center governs the electron cloud distribution, d-orbital energy splitting, and the binding strength with reaction intermediates (e.g., *OH, *O, and *OOH), thereby profoundly influencing the catalytic kinetics [13]. According to crystal field theory, the d-orbitals of transition metal ions in an octahedral crystal field are split into high-energy e_g orbitals and low-energy t_{2g} orbitals [14]. The distribution of spin electrons among these orbitals forms diverse spin states, which exert different regulatory effects on OER activity. For example, Piotr M. Kowalski et al. found that in the Fe-doped NiOOH system, low-spin Fe^{3+} has a similar ionic radius to Ni^{3+}, which not only achieves high solubility of Fe in NiOOH, but also brings the d-band center of Fe closer to the Fermi level, making it a highly active site for OER with better catalytic performance than high-spin Fe^{3+} [15]. Zou et al. triggered the Invar effect via heat value, accelerating electron transfer at the $Fe_{64}Ni_{36}FeNiO_xH_y$ interface, which not only provides a method for thermally induced low-spin Fe, but also releases more unoccupied orbitals to achieve electron transfer without pairing energy [16]. Du et al. modulated the surface electronic structure of pentlandite to shift the Fe spin state from low to high spin, which promoted rapid surface reconstruction and improved OER performance [17]. Zhou et al. constructed a $Ni/MnFe_2O_4$ heterojunction to tune the Ni electronic configuration into a high-spin state, which optimized the OH^- adsorption energy and lowered the reaction energy barrier, resulting in enhanced OER activity [18].

Furthermore, the existence form and dynamic behavior of interfacial water significantly influence the catalytic OER activity. The strong intermolecular interactions among water molecules tend to form a robust hydrogen-bonding network rich in 4-coordinated hydrogen-bonded water (4—HB—H_2O) and 2-coordinated hydrogen-bonded water (2—HB—H_2O), which impedes the translocation of water molecules across the inner Helmholtz plane (IHP) to the catalyst surface and thereby restricts the subsequent processes of water adsorption and dissociation [19, 20]. Notably, the influence of spin-state regulation can extend to the catalyst-electrolyte interface, enabling the dynamic reconstruction of the interfacial water network. The modulation of spin state can alter the surface charge distribution and localized electric field of the catalyst, which in turn promotes the enrichment of free water molecules at the IHP and orients them into a reactive "H-down" configuration, thereby significantly lowering the water activation energy barrier [21]. For instance, Ma et al. utilized V-doping to induce a transition of Co^{3+} from a low-spin to a high-spin state in spinel Co_3O_4, which not only effectively modulated the interfacial microenvironment, but also enhanced the adsorption of key intermediates, thereby ultimately optimizing the reaction pathway [22]. Consequently, spin state regulation engineering serves as a dual-effect strategy that simultaneously optimizes the intrinsic adsorption properties of active sites and the microstructure of interfacial water, thereby significantly improving OER performance.

Based on the aforementioned research background, this study proposes a dual-ligand competition strategy with Ni as the metal center. By leveraging the competitive coordination of H_2BDC and H_2TDC ligands, the spin state of Ni in Ni-MOF was delicately modulated, successfully converting the intermediate-spin Ni^{2+} to high-spin Ni^{3+}. This spin state regulation optimizes the adsorption of key intermediates and facilitating oxygen release, but also regulates the interfacial water structure by altering the surface electronic environment to promote free water enrichment. Accordingly, the optimized Ni-$TDC_{0.6}BDC_{0.4}$ catalyst exhibits excellent OER performance, with an overpotential of 230 mV at 10 mA cm^{-2} and a Tafel slope of 53.3 mV dec^{-1}. When implemented in practical devices, the AEMWE system assembled with this catalyst as the anode and commercial Pt/C as the cathode achieves 1.5 A cm^{-2} at cell voltages of only 2.40 (25°C) and 2.07 V (60°C), outperforming conventional RuO_2-based AEMWE system. Furthermore, the Ni-$TDC_{0.6}BDC_{0.4}$-based AEMWE system can operate stably for 500 h at 300 mA cm^{-2} at 25°C. Moreover, the unbiased photovoltaic-driven OWS system integrating this catalyst with commercial solar panels attains a solar-to-hydrogen efficiency of 13.23% and demonstrates outstanding stability under intermittent illumination. This work not only pioneers a new avenue for spin-state modulation of metal-based catalysts, but also underpins the translation of high-efficiency water electrolysis technologies toward industrial-scale green hydrogen production.

2 | Results and Discussion

The schematic synthesis of Ni-$TDC_{0.6}BDC_{0.4}$ is illustrated in Figure 1a, where defect-rich Ni-$TDC_{0.6}BDC_{0.4}$ ultrathin nanosheets were synthesized on carbon fiber paper (CFP)

15213773, 2026, 23, Downloaded from https://onlinelibrary.wiley.com/doi/10.1002/anie.9878440 by Xinlin Yang - South University Of Science , Wiley Online Library on [02/06/2026]. See the Terms and Conditions (https://onlinelibrary.wiley.com/terms-and-conditions) on Wiley Online Library for rules of use; OA articles are governed by the applicable Creative Commons License

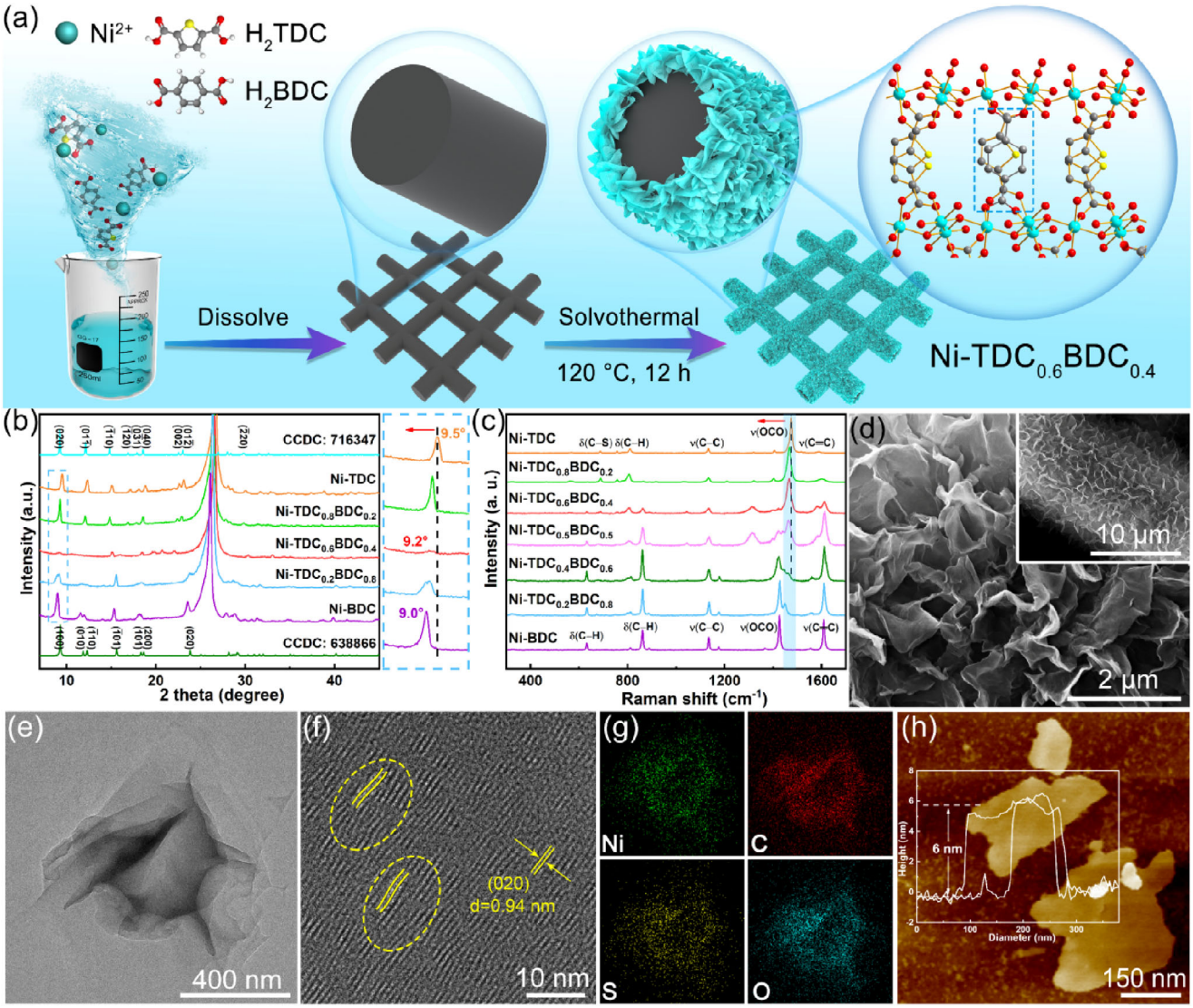

FIGURE 1 | Morphological and structural analysis. (a) Schematic of the synthesis of Ni-TDC$_{0.6}$BDC$_{0.4}$ nanosheets. (b) XRD patterns. (c) Raman spectra. (d) SEM, (e) TEM, (f) HRTEM, (g) corresponding element mapping, and (h) AFM images of Ni-TDC$_{0.6}$BDC$_{0.4}$.

substrate via a mild one-step hydrothermal method using H_2TDC and H_2BDC as the ligand molecules and $Ni(NO_3)_2{\cdot}6H_2O$ as the metal source. Given that Ni-TDC and Ni-BDC exhibit exceedingly similar and multiplicative lattice constants (Figure S1a,b), a proper competitive coordination effect occurs during their coordination process, allowing subtle lattice strains to be introduced into the MOF structure without disrupting its regularity. The schematic structure of Ni-TDC$_{0.6}$BDC$_{0.4}$ is delineated in Figure S1c. Since the molecular length of H_2BDC is longer than that of H_2TDC, incorporating H_2BDC into Ni-TDC may trigger lattice expansion within the MOF, generating numerous unsaturated Ni sites [23], and modifying the coordination environment of Ni atoms, thereby leading to the elongation of the Ni—O bond. As delineated in Figure 1b, the x-ray powder diffraction (XRD) patterns of Ni-TDC and Ni-BDC align perfectly with the corresponding theoretical XRD simulations (CCDC: 716347 and CCDC: 638866) [24, 25], confirming the successful synthesis of Ni-TDC and Ni-BDC. Notably, when H_2BDC is introduced into Ni-TDC, the (020) crystal plane of Ni-TDC at 9.5° gradually shifts to a lower angle (9.0°), indicating the existence of lattice expansion in Ni-TDC$_x$BDC$_{1-x}$. As the H_2BDC content increases, the crystal plane intensity in Ni-TDC$_x$BDC$_{1-x}$ decreases and then increases, with Ni-TDC$_{0.6}$BDC$_{0.4}$ exhibiting the weakest intensity, suggesting the most vigorous ligand competition and the highest degree of tensile strain. Raman spectroscopy was employed to further explore the lattice and strain characteristics in Ni-TDC$_x$BDC$_{1-x}$ (Figure 1c). The Raman characteristic peaks of the synthesized Ni-TDC and Ni-BDC correspond well with the previously reported MOFs, respectively [26, 27]. Notably, Ni-TDC$_{0.6}$BDC$_{0.4}$ displays a new sharp peak at 862 cm^{-1}, attributed to the C—H bending vibration of the H_2BDC plane, confirming the successful introduction of the H_2BDC ligand. Furthermore, the stretching vibration peak of the carboxylic acid group (COO^-) in Ni-TDC$_{0.6}$BDC$_{0.4}$ is red-shifted from 1474 to 1460 cm^{-1} compared to Ni-TDC, providing additional evidence of lattice strain formation [28].

The morphology and microstructure of Ni-TDC$_{0.6}$BDC$_{0.4}$ were examined using scanning electron microscopy (SEM) and transmission electron microscopy (TEM). As disclosed in Figure 1d,e,

15213773, 2026, 23, Downloaded from https://onlinelibrary.wiley.com/doi/10.1002/anie.9878440 by Xinlin Yang - South University Of Science , Wiley Online Library on [02/06/2026]. See the Terms and Conditions (https://onlinelibrary.wiley.com/terms-and-conditions) on Wiley Online Library for rules of use; OA articles are governed by the applicable Creative Commons License

Ni-TDC$_{0.6}$BDC$_{0.4}$ exhibits ultrathin 2D nanosheet morphology, with the flexible nanosheets curling spontaneously at the edges. Compared to the 3D stacked structures of other comparative samples (Figure S2a,b), the unique nanosheet structure of Ni-TDC$_{0.6}$BDC$_{0.4}$ can furnish the larger specific surface area, more active sites and faster mass transfer rate. The high-resolution TEM (HRTEM) image reveals the lattice fringe of 0.94 nm corresponding to the (020) crystal plane of Ni-TDC$_{0.6}$BDC$_{0.4}$ (Figure 1f). It is noteworthy that the distorted lattice fringe regions are also observed, which further affirms the presence of lattice strain in Ni-TDC$_{0.6}$BDC$_{0.4}$. The occurrence of lattice strain likely induces the formation of lattice defects, which can expose affluent active sites and promote the OER process [29]. Additionally, the elemental mapping images of Ni-TDC$_{0.6}$BDC$_{0.4}$ show the uniform distribution of Ni, C, O, and S elements (Figure 1g), indicating that introducing the H_2BDC ligand does not result in non-uniform coordination between ligand functional groups and metal ions. Atomic force microscopy (AFM) image (Figure 1h) displays that the thickness of Ni-TDC$_{0.6}$BDC$_{0.4}$ ultrathin nanosheet is approximately 6 nm. For comparison, SEM and TEM images of Ni-TDC and Ni-BDC are presented in Figures S3, S4, respectively. The distinct Bragg reflection spots in the SAED patterns confirm the high crystallinity of Ni-TDC and Ni-BDC. Furthermore, the elemental mapping images reveal the uniform distribution of elements, verifying the successful synthesis of Ni-TDC and Ni-BDC.

Thermogravimetric analysis (TGA) results of Ni-TDC$_{0.6}$BDC$_{0.4}$, Ni-TDC and Ni-BDC are presented in Figure S5. The pyrolysis process of catalysts is divided into three phases. Specifically, the first weight loss (0-210°C) of Ni-TDC$_{0.6}$BDC$_{0.4}$ corresponds to the departure of absorbed water (H_2O_{ads}) and DMF. The second weight loss (210-285°C) is attributed to the thermal decomposition of the Ni-TDC$_{0.6}$BDC$_{0.4}$ organic skeleton. The third weight loss (285-550°C) is due to the complete carbonization of Ni-TDC$_{0.6}$BDC$_{0.4}$ [30]. Notably, the thermal decomposition temperature of organic skeleton of Ni-TDC$_{0.6}$BDC$_{0.4}$ is significantly lower than that of Ni-TDC and Ni-BDC, suggesting the presence of defects between the ligand and the metal in Ni-TDC$_{0.6}$BDC$_{0.4}$ [30]. The pore structure and specific surface area of catalysts were analyzed by nitrogen isothermal adsorption and desorption curves. As demonstrated in Figure S6a,b, Ni-TDC$_{0.6}$BDC$_{0.4}$, Ni-TDC and Ni-BDC all display type II isotherms with H3-type hysteresis loops. The pore diameters of Ni-TDC and Ni-BDC are 20.9 and 25.7 nm, respectively. In contrast, Ni-TDC$_{0.6}$BDC$_{0.4}$ possesses a reduced pore diameter of 7.4 nm, which is characteristic of the mesoporous architecture. Notably, the BET surface area of Ni-TDC$_{0.6}$BDC$_{0.4}$ reaches 47.5 $m^2\ g^{-1}$, which is substantially higher than that of Ni-TDC (2.1 $m^2\ g^{-1}$) and Ni-BDC (3.6 $m^2\ g^{-1}$). These results attest that the lattice strain and presence of defects not only modify the coordination structure of Ni atoms, but also increase the specific surface area of Ni-TDC$_{0.6}$BDC$_{0.4}$.

The electrocatalytic OER performance of catalysts was evaluated using a conventional three-electrode system in 1.0 M KOH solution at room temperature, with all recorded potentials calibrated to the reversible hydrogen electrode (RHE). As depicted in Figure 2a, Ni-TDC$_{0.6}$BDC$_{0.4}$ exhibits a higher oxidation peak than Ni-TDC and Ni-BDC, indicating that the Ni species in Ni-TDC$_{0.6}$BDC$_{0.4}$ are more readily oxidized to the high-valence and active Ni^{3+} state [31, 32]. More importantly, Ni-TDC$_{0.6}$BDC$_{0.4}$ exhibits outstanding OER activity, requiring only low overpotentials of 230 and 316 mV to achieve current densities of 10 and 100 mA cm^{-2}, respectively, which surpass that of other control samples. To further investigate the reaction kinetics and eliminate interference from oxidation peaks, the Tafel slope was accurately determined using reverse LSV data (Figure S7). As depicted in Figure 2b, the Tafel slope (53.3 mV dec^{-1}) of Ni-TDC$_{0.6}$BDC$_{0.4}$ is significantly lower than that of the other reference samples, demonstrating the superior rapid reaction kinetics of Ni-TDC$_{0.6}$BDC$_{0.4}$. Additionally, the overpotential and Tafel slope of Ni-TDC$_{0.6}$BDC$_{0.4}$ transcend those of most previously reported high-performance MOF-based OER catalysts (Figure 2c and Table S1). Electrochemical impedance spectroscopy (EIS) was employed to evaluate the charge transfer capacity of catalysts. According to the Nyquist plots (Figure 2d), Ni-TDC$_{0.6}$BDC$_{0.4}$ displays a low charge transfer resistance (R_{ct}) of 0.87 Ω, which is lower than that of Ni-TDC (1.34 Ω), Ni-TDC$_{0.8}$BDC$_{0.2}$ (0.93 Ω), Ni-TDC$_{0.2}$BDC$_{0.8}$ (1.54 Ω) and Ni-BDC (1.58 Ω), verifying that Ni-TDC$_{0.6}$BDC$_{0.4}$ possesses the faster charge transfer rate [33]. The electrochemical double-layer capacitance (C_{dl}) was calculated from the cyclic voltammetry (CV) curves in the non-Faraday region (Figure S8) to estimate the electrochemical active surface area (ECSA) of catalysts. As seen in Figure 2e, Ni-TDC$_{0.6}$BDC$_{0.4}$ exhibits the largest C_{dl} of 2.41 mF cm^{-2}, surpassing than that of Ni-TDC (1.23 mF cm^{-2}), Ni-TDC$_{0.8}$BDC$_{0.2}$ (0.39 mF cm^{-2}), Ni-TDC$_{0.2}$BDC$_{0.8}$ (0.49 mF cm^{-2}), and Ni-BDC (0.30 mF cm^{-2}), indicating that Ni-TDC$_{0.6}$BDC$_{0.4}$ possesses the largest ECSA. The turnover frequency (TOF) based on ICP-MS results (Table S2) and the mass-specific activity (MA) were calculated to assess the intrinsic activity of catalysts. As shown in Figure 2f, the TOF value of Ni-TDC$_{0.6}$BDC$_{0.4}$ exceeds that of other catalysts at the same potential. Additionally, Ni-TDC$_{0.6}$BDC$_{0.4}$ exhibits the highest MA value (Figure 2g). These results demonstrate Ni-TDC$_{0.6}$BDC$_{0.4}$ possesses excellent OER conversion efficiency and prominent intrinsic catalytic activity [34]. Moreover, the stability of Ni-TDC$_{0.6}$BDC$_{0.4}$ was evaluated to appraise its practical application potential. As depicted in Figure 2h, the chronopotentiometry stability test results demonstrate the remarkable durability of Ni-TDC$_{0.6}$BDC$_{0.4}$, which can continuously operate for 100 h at 10 and 100 mA cm^{-2} without significant change in overpotential.

X-ray photoelectron spectroscopy (XPS) was used to analyze the surface composition and chemical state of catalysts. The XPS survey spectra display the presence of Ni, C, O, and S elements in Ni-TDC$_{0.6}$BDC$_{0.4}$ (Figure S9), which is consistent with the elemental mapping analysis described above. The high-resolution O 1s XPS spectra are presented in Figure S10a. For Ni-TDC$_{0.6}$BDC$_{0.4}$, it can be divided into four peaks of the M—O (530.0 eV), oxygen vacancies (O_v, 531.3 eV), C—O (532.0 eV), and adsorbed water (H_2O_{ads}, 533.0 eV). Notably, the C—O bond binding energy in Ni-TDC$_{0.6}$BDC$_{0.4}$ exhibits a distinct shift relative to that in Ni-TDC and Ni-BDC. This trend can be attributed to the altered coordination environment of ligand-bonded O atoms, which arises from the competitive coordination effect between the dual ligands. The M—O bond in Ni-TDC$_{0.6}$BDC$_{0.4}$ shifts to lower binding energy, implying that the dual-ligand strategy facilitates greater electron transfer from Ni to O atoms [35]. High-resolution XPS of Ni 2p was used to explore the electronic structure changes of Ni atoms (Figure S10b). For Ni-TDC and Ni-BDC, the Ni $2p_{3/2}$ peaks are primarily composed of Ni^{2+} (855.8 eV) and satellite

15213773, 2026, 23, Downloaded from https://onlinelibrary.wiley.com/doi/10.1002/anie.9878440 by Xinlin Yang - South University Of Science , Wiley Online Library on [02/06/2026]. See the Terms and Conditions (https://onlinelibrary.wiley.com/terms-and-conditions) on Wiley Online Library for rules of use; OA articles are governed by the applicable Creative Commons License

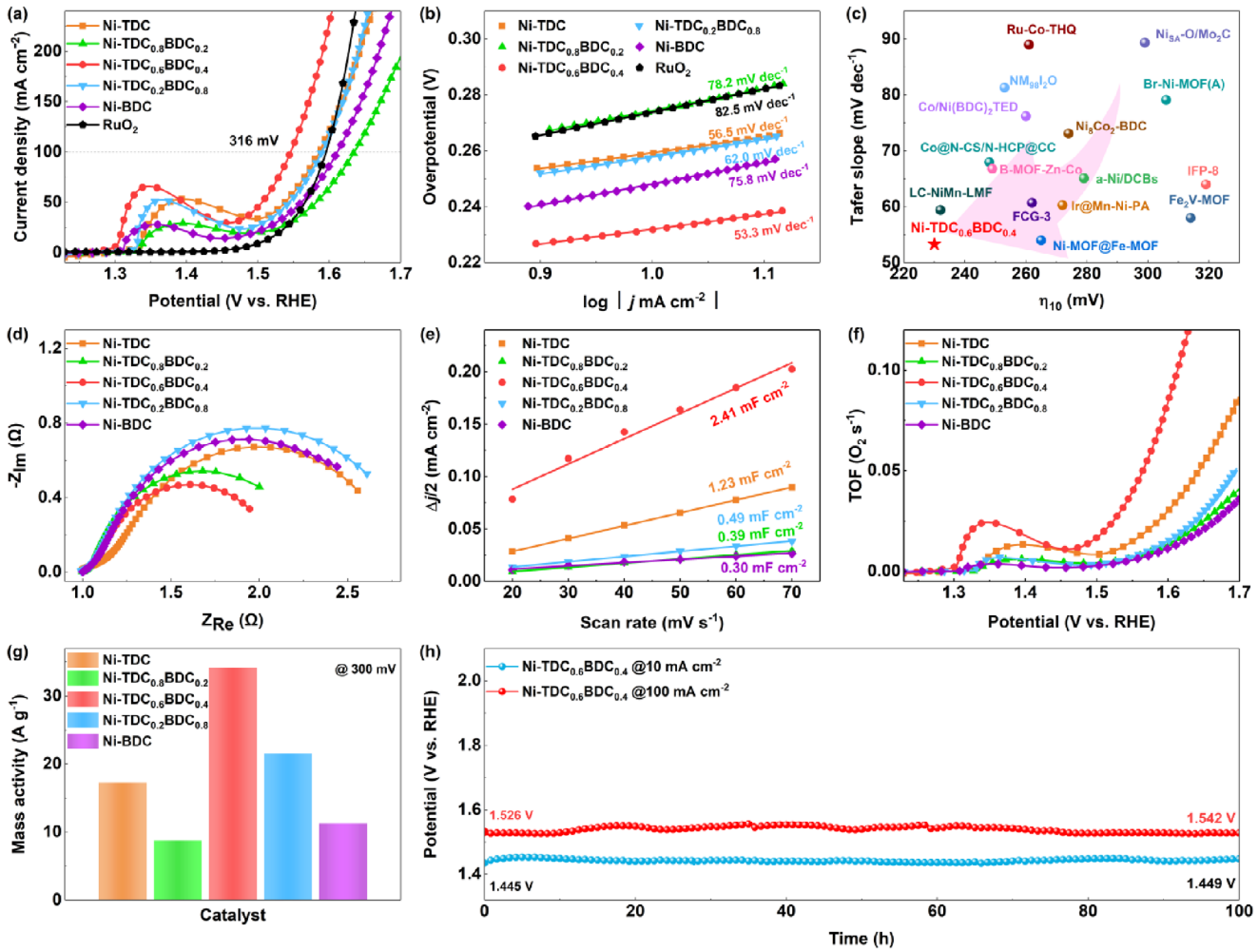

FIGURE 2 | Electrocatalytic OER tests in 1.0 M KOH solution. (a) LSV polarization curves. (b) Tafel slopes. (c) Comparison of the overpotential at 10 mA cm^{-2} and Tafel slope with previously reported catalysts. (d) Nyquist plots. (e) C_{dl} plots. (f) TOF curves. (g) OER mass activity at 300 mV. (h) Chronopotentiometry of Ni-$TDC_{0.6}BDC_{0.4}$ at 10 and 100 mA cm^{-2}.

peaks (861.4 eV, Sat.) [36]. Additionally, Ni-$TDC_{0.6}BDC_{0.4}$ displays a discernible shoulder at 857.1 eV, a hallmark of high-valent Ni^{3+}. This observation indicates that the introduction of dual ligands modulates the electronic structure of Ni atoms, generating both saturated and unsaturated Ni sites [37].

Electron paramagnetic resonance (EPR) technique was utilized to detect the existence of oxygen vacancies in Ni-$TDC_{0.6}BDC_{0.4}$ (Figure 3a). Ni-$TDC_{0.6}BDC_{0.4}$ exhibits a broadened and pronounced peak at $g = 2.003$ compared to Ni-TDC and Ni-BDC, indicating that Ni-$TDC_{0.6}BDC_{0.4}$ incorporates abundant oxygen vacancies and unpaired electrons [38]. This can be attributed to dual-ligand competitive coordination disrupting the symmetric coordination environment of single-ligand MOFs, weakening/cleaving Ni—O bonds and rendering lattice O atoms more prone to detachment, thereby facilitating oxygen vacancy formation. Oxygen vacancies generate abundant local electrons that effectively modulate the electronic states of metal atoms, furnish active sites for catalysis, and strongly attract active molecules, thereby enhancing catalytic activity [39]. The local structure of Ni in Ni-$TDC_{0.6}BDC_{0.4}$ was investigated by Ni K-edge x-ray absorption spectroscopy. The Ni K-edge x-ray absorption near-edge structure (XANES) spectrum of Ni-$TDC_{0.6}BDC_{0.4}$ exhibits a higher absorption edge compared to that of Ni-BDC and Ni-TDC (Figure 3b), signifying an elevated oxidation state of Ni in Ni-$TDC_{0.6}BDC_{0.4}$, which is consistent with previous XPS results [40, 41]. The pre-edge peak at 8340–8330 eV is associated with the electric quadrupole transition from the 1s orbital to the 3d orbital, where the peak intensity reflects the number of unoccupied orbitals [42]. Compared with Ni-TDC and Ni-BDC, Ni-$TDC_{0.6}BDC_{0.4}$ exhibits higher pre-edge peak intensity, indicating a stronger orbital affinity of the 3d orbital for transition electrons. Consequently, it is inferred that the Ni atoms in Ni-$TDC_{0.6}BDC_{0.4}$ possess more semi-full orbitals and unpaired electrons. Concurrently, the white line peak of Ni-$TDC_{0.6}BDC_{0.4}$ is broadening and weakening features, implying a greater extent of splitting of the Ni 4p orbitals and the reduction of the Ni—O coordination number in Ni-$TDC_{0.6}BDC_{0.4}$ [43]. As demonstrated in Figure S11, the Ni K-edge $k^3\chi$ data for the extended x-ray absorption fine structure (EXAFS) oscillations of Ni-$TDC_{0.6}BDC_{0.4}$ showcases smaller amplitude oscillations compared to Ni-TDC and Ni-BDC, confirming that the Ni sites in Ni-$TDC_{0.6}BDC_{0.4}$ have slight structural distortion and a lower average coordination number (CN) [44]. The Fourier transform (FT) of Ni K-edge EXAFS spectra of Ni-TDC, Ni-BDC and Ni-$TDC_{0.6}BDC_{0.4}$ appear a characteristic peak at about 1.5 Å (Figure 3c), corresponding to

15213773, 2026, 23, Downloaded from https://onlinelibrary.wiley.com/doi/10.1002/anie.9878440 by Xinlin Yang - South University Of Science , Wiley Online Library on [02/06/2026]. See the Terms and Conditions (https://onlinelibrary.wiley.com/terms-and-conditions) on Wiley Online Library for rules of use; OA articles are governed by the applicable Creative Commons License

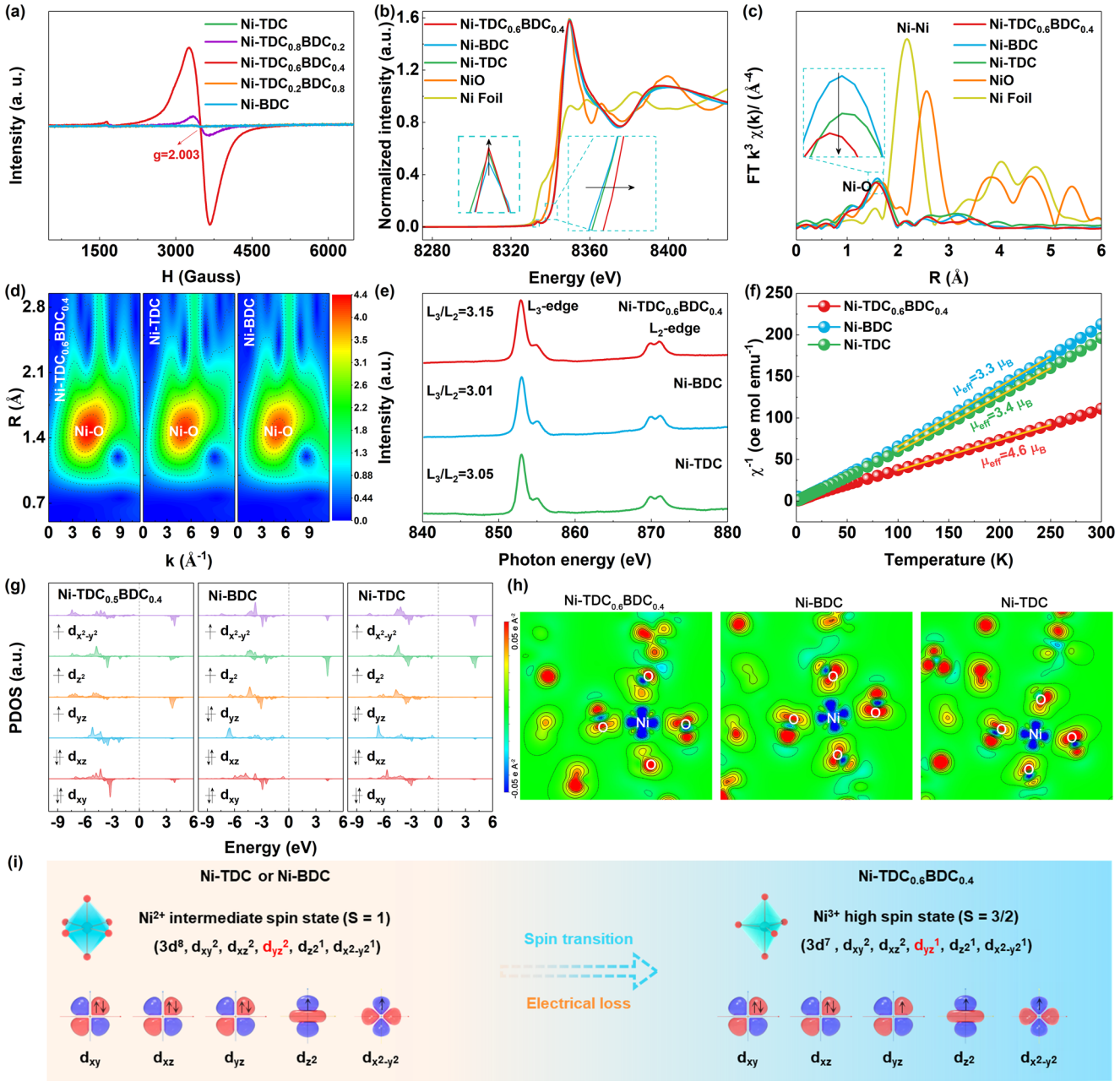

FIGURE 3 | Valence state and spin configuration analysis. (a) EPR spectra. (b) Ni K-edge XANES spectra. (c) Ni K-edge EXAFS spectra in R-space. (d) The WT contour plots for the k^3-weighted EXAFS signal. (e) Ni L-edge XANES spectra. (f) χ^{-1}-T plots. (g) Calculated PDOS of Ni-3d orbitals. (h) The charge density difference. The red and blue areas respectively represent the gain of electrons and the loss of electrons and the unit range is from 0.05 to -0.05 Å e^{-2}. (i) Schematic diagram of electron spin change.

the Ni—O coordination, which is also confirmed by the wavelet transform (WT) results (Figure 3d) [45]. Additionally, the decline in Ni—O peak intensity in Ni-$TDC_{0.6}BDC_{0.4}$ corroborates the increased extent of NiO_6 octahedron distortion [46]. The EXAFS curve fitting analysis reveals that the average CN of Ni (5.6) in Ni-$TDC_{0.6}BDC_{0.4}$ is smaller than that of Ni-TDC (6.0) and Ni-BDC (6.0) (Figures S12a–c and Table S3), indicating the presence of unsaturated Ni sites in Ni-$TDC_{0.6}BDC_{0.4}$. Interestingly, the unsaturated coordination leads to a longer bond length of the Ni—O bond in Ni-$TDC_{0.6}BDC_{0.4}$ (2.05 Å) than in Ni-TDC (2.03 Å) and Ni-BDC (2.03 Å). The above results imply that introducing the dual ligands alters the local coordination geometry of Ni with decreased number of coordinated O, thereby forming numerous unsaturated Ni sites and oxygen vacancies in Ni-$TDC_{0.6}BDC_{0.4}$.

Furthermore, we also investigated the evolution of the spin state of Ni sites. As shown in Figure 3e, the Ni L-edge XANES spectrum exhibits two characteristic L_3-edge and L_2-edge peaks. Previous reports indicate a positive correlation between the area ratios of L_3/L_2 and spin state [47]. The Ni L-edge XANES spectrum of Ni-$TDC_{0.6}BDC_{0.4}$ shows an L_3/L_2 area ratio of 3.15, higher than that of Ni-TDC (3.05) and Ni-BDC (3.01), indicating the higher spin state of Ni in Ni-$TDC_{0.6}BDC_{0.4}$. Additionally, the hysteresis loops of catalysts were collected using a superconducting quantum

15213773, 2026, 23, Downloaded from https://onlinelibrary.wiley.com/doi/10.1002/anie.9878440 by Xinlin Yang - South University Of Science , Wiley Online Library on [02/06/2026]. See the Terms and Conditions (https://onlinelibrary.wiley.com/terms-and-conditions) on Wiley Online Library for rules of use; OA articles are governed by the applicable Creative Commons License

interference device. As shown in Figure S13a, Ni-TDC$_{0.6}$BDC$_{0.4}$ exhibits a steeper slope than Ni-TDC and Ni-BDC, further demonstrating enhanced magnetism and altered spin states at Ni sites following the introduction of the dual ligands [48]. We employed zero-field cooling temperature-dependent (ZFC-T) magnetic susceptibility (χm) measurement to further investigate the spin state changes at Ni sites in Ni-TDC$_{0.6}$BDC$_{0.4}$, Ni-TDC and Ni-BDC (Figures S13b and 3f). The total effective magnetic moment (μ_{eff}) was calculated from the inverse susceptibility (χ^{-1}) versus temperature (T) plots. The μ_{eff} value of Ni-TDC$_{0.6}$BDC$_{0.4}$ (4.6 μ_B) is higher than that of Ni-TDC (3.4 μ_B) and Ni-BDC (3.3 μ_B), revealing that introducing dual ligands induces a higher spin state in Ni-TDC$_{0.6}$BDC$_{0.4}$ than in Ni-TDC and Ni-BDC [48]. Based on the equation $\sqrt{8C}\ \mu_B = \mu_{eff} = \sqrt{n(n+2)}\ \mu_B$ [49], the number of unpaired electrons (n) of was evaluated as ~3.6, ~2.6, and ~2.5 for Ni-TDC$_{0.6}$BDC$_{0.4}$, Ni-TDC and Ni-BDC, respectively. This outcome indicates a greater number of unpaired electrons in Ni-TDC$_{0.6}$BDC$_{0.4}$.

To further analyze the electronic structure characteristics of Ni sites, we calculated the projected density of states (PDOS) for Ni 3d in Ni-TDC$_{0.6}$BDC$_{0.4}$, Ni-TDC, and Ni-BDC. Theoretically, the electrons of Ni ions can be arranged in five 3d orbitals (d_{xy}, d_{xz}, d_{yz} , d_{z^2}, $d_{x^2-y^2}$) with different occupation patterns, thereby producing distinct electronic spin states. As shown in Figure 3g, the unoccupied orbitals in Ni-TDC$_{0.6}$BDC$_{0.4}$ mainly included, d_{z^2} and $d_{x^2-y^2}$, with an electronic configuration of $d_{xy}^{\ 2}$, $d_{xz}^{\ 2}$, $d_{yz}^{\ 1}$, $d_{z^2}^{\ 1}$, $d_{x^2-y^2}^{\ 1}$, corresponding to Ni^{3+} in a high spin state. In contrast, the unoccupied orbitals above the Fermi level in Ni-TDC and Ni-BDC are mainly d_{z^2} and $d_{x^2-y^2}$, with an electronic configuration of $d_{xy}^{\ 2}$, $d_{xz}^{\ 2}$, $d_{yz}^{\ 2}$, $d_{z^2}^{\ 1}$, $d_{x^2-y^2}^{\ 1}$, corresponding to Ni^{2+} in an intermediate-spin state. Additionally, we calculated the charge density difference of the samples. As seen in Figure 3h, the blue region surrounding Ni sites in Ni-TDC$_{0.6}$BDC$_{0.4}$ is more extensive than that of Ni-TDC and Ni-BDC, suggesting greater electron loss in Ni-TDC$_{0.6}$BDC$_{0.4}$. The results demonstrate that the dual-ligand effect induces the reconstruction of the electronic structure at Ni sites, increasing the number of unpaired electrons and the active state density of 3d orbitals, thereby forming high-spin Ni^{3+} and unsaturated sites. Figure 3i clearly contrasts the spin states and 3d orbital electron configurations of Ni sites in single-ligand MOFs (Ni-TDC and Ni-BDC) versus the dual-ligand Ni-TDC$_{0.6}$BDC$_{0.4}$. For Ni-TDC and Ni-BDC, Ni^{2+} exhibits an intermediate spin state ($S = 1$) with the 3d electron configuration of $d_{xy}^{\ 2}$, $d_{xz}^{\ 2}$, $d_{yz}^{\ 2}$, $d_{z^2}^{\ 1}$, $d_{x^2-y^2}^{\ 1}$, accompanied by the symmetric distribution of d-orbital electrons. In Ni-TDC$_{0.6}$BDC$_{0.4}$, Ni^{3+} adopts a high-spin state ($S = 3/2$) with the 3d orbital arrangement of $d_{xy}^{\ 2}$, $d_{xz}^{\ 2}$, $d_{yz}^{\ 1}$, $d_{z^2}^{\ 1}$, $d_{x^2-y^2}^{\ 1}$, which possesses three singly occupied orbitals that can act as selective gates and facilitate the transfer of local spin current [50].

To investigate the surface reconstruction process of the catalysts during the OER process, the structural evolution of Ni-TDC$_{0.6}$BDC$_{0.4}$, Ni-TDC, and Ni-BDC was analyzed by electrochemical in situ Raman spectroscopy in the potential range of 1.00–1.60 V (vs. RHE) (Figure S14). As seen in Figure 4a, a new peak appears at 486 cm^{-1} when the applied voltage reaches 1.30 (V vs. RHE). This peak is attributed to the A_{1g} stretching vibration of Ni^{II}—O in $Ni(OH)_2$ [51], predicting the transition of Ni-TDC$_{0.6}$BDC$_{0.4}$ to NiOOH active species, which coincides with the oxidation peak potential observed in the LSV curve. Significantly, Ni-TDC$_{0.6}$BDC$_{0.4}$ exhibits a lower transition potential (1.30 V vs. RHE) than that of Ni-TDC (1.36 V vs. RHE) and Ni-BDC (1.34 V vs. RHE) (Figures S15–S16), indicating that the high-spin Ni species in Ni-TDC$_{0.6}$BDC$_{0.4}$ enable faster oxidative reconstruction, leading to the formation of highly active metal hydroxides. Furthermore, when the applied voltage reaches 1.36 (V vs. RHE), two new sharp peaks emerge at 474 and 555 cm^{-1}, corresponding to the E_g bending vibration and A_{1g} stretching vibration of Ni^{III}—O bond in NiOOH, respectively [52]. As the applied voltage increases, the peak at 486 cm^{-1} gradually redshifts to 474 cm^{-1}, indicating the transition process from Ni^{II}—O to Ni^{III}—O [53]. Crucially, the relative intensities of characteristic peaks at 474 and 555 cm^{-1} reflect the phase transition of NiOOH. The peak intensity at 555 cm^{-1} is more substantial than that at 474 cm^{-1}, indicating a higher proportion of β-NiOOH [54, 55]. Compared to γ-NiOOH, β-NiOOH possesses a higher oxidation state, resulting in the better OER intrinsic activity [56, 57]. Subsequently, in situ attenuated total reflection-surface enhanced infrared absorption spectroscopy (ATR-SEIRAS) was utilized to study the adsorption of oxygen intermediates on Ni-TDC$_{0.6}$BDC$_{0.4}$ (high-spin Ni^{3+} sites), Ni-TDC, and Ni-BDC (both with intermediate-spin Ni^{2+} sites) during the OER process. As presented in Figures 4b and S17–18, the in situ ATR-SEIRAS spectra of Ni-TDC$_{0.6}$BDC$_{0.4}$, Ni-TDC, and Ni-BDC progressively evolve as the applied potential is increased. The absorption peaks at 1250 and 3400 cm^{-1} is assigned to the stretching vibrations of O—O in *OOH and O—H in *OH intermediates, respectively [58]. This validates that the OER process of Ni-TDC$_{0.6}$BDC$_{0.4}$ proceeds via the conventional adsorbate evolution mechanism (AEM) pathway [59]. Notably, the adsorption intensities of key *OOH and *OH intermediates on Ni-TDC$_{0.6}$BDC$_{0.4}$ are significantly higher than those on Ni-TDC and Ni-BDC with increasing applied potential (Figure 4c), reflecting that Ni-TDC$_{0.6}$BDC$_{0.4}$ possesses faster oxygen exchange kinetics [60]. Therefore, the high-spin Ni^{3+} sites enables significantly enhanced adsorption of key oxygen intermediates (*OOH and *OH) due to its richer unpaired electrons and higher 3d orbital active state density, which accelerates oxygen exchange kinetics and underpins efficient active sites for OER.

To further elucidate the origin of the outstanding OER performance and structural advantages of Ni-TDC$_{0.6}$BDC$_{0.4}$, in situ XAS technique was utilized to study the dynamic evolution of local coordination environment and oxidation state under OER-associated potentials. In situ XANES spectra were measured at the open-circuit potential (OCP), 1.20, 1.30, and 1.50 V (vs. RHE) (Figures 4d and S19). As displayed in the Ni K-edge XANES spectra of Ni-TDC$_{0.6}$BDC$_{0.4}$ and Ni-BDC, the absorption edge gradually shifts toward higher energy with increasing applied potential, indicating the oxidation of Ni species ($Ni^{2+} \rightarrow Ni^{3+}$) [61]. Generally, the elevation of metal valence state is a consequence of the deprotonation process during OER [62]. The presence of high-spin Ni sites is liable to promote the adsorption of OH^- ions on the active centers to form the adsorbed M—OH species. Subsequently, this facilitates the deprotonation process at relatively low potentials, thereby enabling the generation of active oxygen species (M—OOH) on the surface. Furthermore, the alterations in the coordination number and local interatomic distance were derived from extended EXAFS curve-fitting analysis (Figures 4e and S20). As illustrated in Figure 4f,g and

15213773, 2026, 23, Downloaded from https://onlinelibrary.wiley.com/doi/10.1002/anie.9878440 by Xinlin Yang - South University Of Science , Wiley Online Library on [02/06/2026]. See the Terms and Conditions (https://onlinelibrary.wiley.com/terms-and-conditions) on Wiley Online Library for rules of use; OA articles are governed by the applicable Creative Commons License

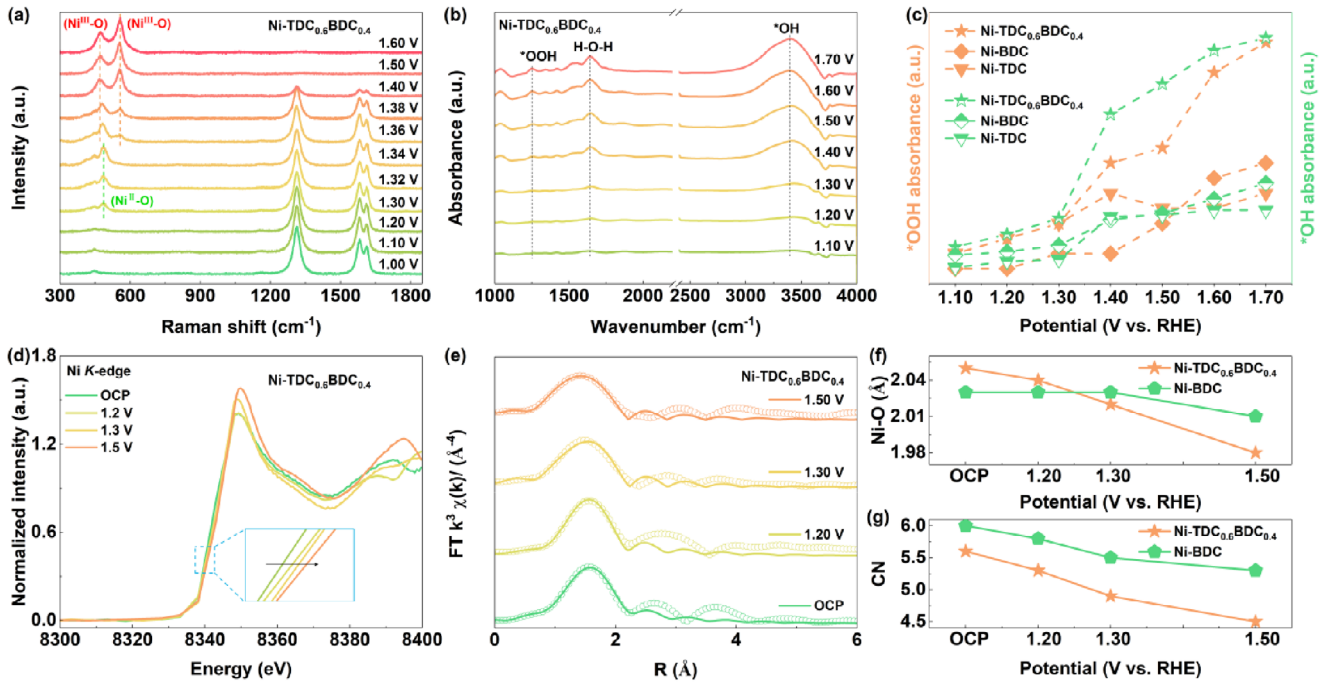

FIGURE 4 | Catalyst structure evolution analysis. (a) In situ Raman spectra. (b) In situ ATR-SEIRAS spectra. (c) Comparison of the adsorption intensities of *OOH and *OH intermediates at different potentials. (d) In situ Ni K-edge XANES spectra. (e) Corresponding Ni K-edge EXAFS fitting curves in R space from (d). (f) Ni—O bond distances and (g) CN corresponding to R space.

Tables S4, S5, the Ni—O bond distances and average CN of the samples were determined by R-space fitting of the first coordination shell. The Ni—O bond distance of Ni-$TDC_{0.6}BDC_{0.4}$ contracts from 2.05 Å at OCP to 1.98 Å at higher potentials, reflecting lattice contraction induced by oxidation [63]. Notably, the contraction rate of the Ni—O bond distance with increasing potential for Ni-$TDC_{0.6}BDC_{0.4}$ is significantly faster than that for Ni-BDC, indicating that Ni-$TDC_{0.6}BDC_{0.4}$ undergoes more rapid oxidative reconstruction to form the active NiOOH phase. Additionally, a more pronounced decrease in CN is observed for Ni-$TDC_{0.6}BDC_{0.4}$ compared to Ni-BDC under applied potentials, which can be attributed to the rapid dissociation of dual ligands and the prompt replacement of partial hydroxyl/water species at high positive potentials. Collectively, these results demonstrate that the presence of high-spin Ni^{3+} sites enable Ni-$TDC_{0.6}BDC_{0.4}$ to undergo faster transformation into the high-oxidation-state NiOOH phase during OER.

In order to further understand the impact of spin state changes on the catalysts, Ni-$TDC_{0.6}BDC_{0.4}$ after OER test was characterized by SEM, TEM, and XPS measurements. Ni-$TDC_{0.6}BDC_{0.4}$ after OER test still maintains the nanosheet structure, but its surface becomes rougher (Figure S21a). This increased roughness is more clearly observed in the TEM image (Figure S21b). The HRTEM image (Figure S21c) reveals distinct lattice fringes, with the lattice fringes of 0.71 and 0.23 nm corresponding to the $(01\bar{1})$ crystal plane of Ni-$TDC_{0.6}BDC_{0.4}$ and the (002) crystal plane of NiOOH (PDF# 06-0141), respectively. This observation indicates that the Ni-$TDC_{0.6}BDC_{0.4}$ is partially reconstructed to NiOOH, suggesting that Ni-$TDC_{0.6}BDC_{0.4}$/NiOOH is the actual active species during the OER process. EDX mapping images confirm the uniform distribution of Ni, C, O, and S elements within the nanosheet structure (Figure S21d), and the presence of S element further validates the partial retention of the MOF structure. The Ni 2p XPS spectrum of Ni-$TDC_{0.6}BDC_{0.4}$ after OER test exhibits (Figure S22) that the peaks at 855.7 and 873.5 eV corresponding to Ni^{2+} species, while new peaks at 856.8 and 875.3 eV are attributed to the Ni^{3+} species. Notably, the Ni 2p spectrum of Ni-$TDC_{0.6}BDC_{0.4}$ after OER test shifts 0.45 eV toward higher binding energy, indicating the formation of high-valent NiOOH active species during the OER process [64, 65]. High-valent Ni species feature stronger catalytic activity, which can significantly accelerate the charge transfer with oxygen intermediates, thus dramatically improving OER performance [44, 66]. In the O 1s spectra (Figure S23), the intensity of M—O bond peak decreases after the OER test, signifying that the longer M—O bond resulting from the lattice strain-induced defect strategy contributes to the catalytic reaction [67].

To further elucidate the correlation between the structural evolution of the catalyst-electrolyte interface water in alkaline OER and the spin state of the Ni center, we performed in situ attenuated total reflection-surface enhanced infrared absorption spectroscopy (ATR-SEIRAS) under 1.0 M KOH conditions (Figures 5a and S24a,b). Gaussian fitting was performed in the OH stretching region (3000–3800 cm^{-1}) within the potential range of 1.40–1.70 V (vs. RHE). The green area represents 4-coordination hydrogen-bonded water (4—HB—H_2O), the orange area represents 2-coordination hydrogen-bonded water (2—HB—H_2O), and the blue area represents potassium ion bound to water (K^+—H_2O) or non-hydrogen-bonded water (Free-H_2O) [21]. In general, interfacial H_2O with fewer intramolecular H-bonds is more easily dissociated, so the activation energies of water dissociation increased in the order: K^+—H_2O (Free-H_2O)<2—HB—H_2O<4—HB—H_2O [20]. The relative proportions of three peaks of the catalyst are presented in Figures 5b and S25a,b. During the OER process,

15213773, 2026, 23, Downloaded from https://onlinelibrary.wiley.com/doi/10.1002/anie.9878440 by Xiulin Yang - South University Of Science , Wiley Online Library on [02/06/2026]. See the Terms and Conditions (https://onlinelibrary.wiley.com/terms-and-conditions) on Wiley Online Library for rules of use; OA articles are governed by the applicable Creative Commons License

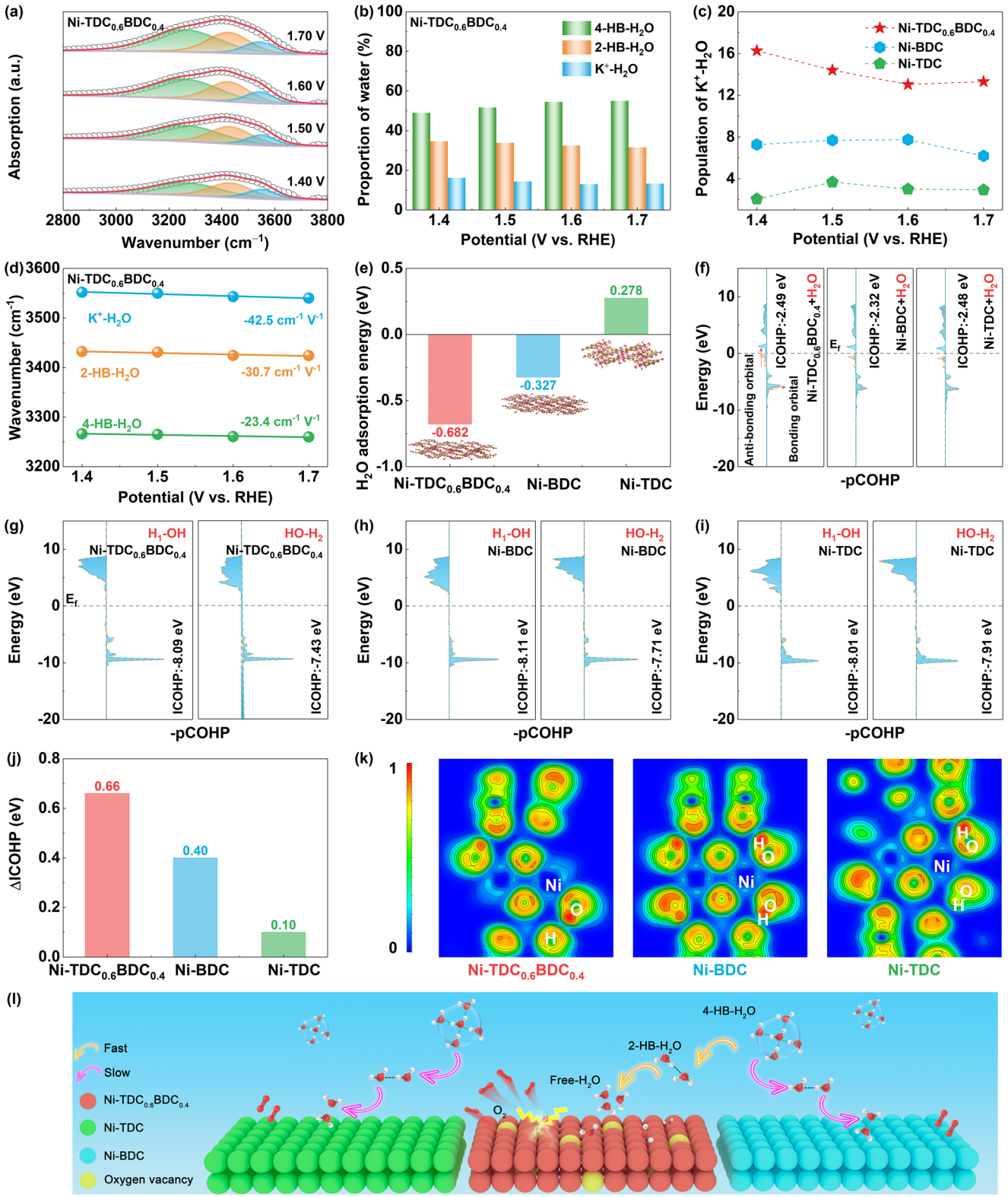

FIGURE 5 | Interfacial water structure of catalysts. (a) In situ ATR-SEIRAS spectra of interfacial water on Ni-$TDC_{0.6}BDC_{0.4}$. Gaussian fitting of three O—H stretching modes of 4—HB—H_2O, 2—HB—H_2O, and K^+—H_2O are shown in green, orange and blue, respectively. (b) The proportions of different types of water for Ni-$TDC_{0.6}BDC_{0.4}$. (c) The proportions of K^+—H_2O at different potentials of Ni-$TDC_{0.6}BDC_{0.4}$, Ni-BDC, and Ni-TDC. (d) Stark slopes for Ni-$TDC_{0.6}BDC_{0.4}$. (e) The water adsorption energy on Ni-$TDC_{0.6}BDC_{0.4}$, Ni-BDC and Ni-TDC surfaces. (f) pCOHP between the O atom of the adsorbed H_2O and the Ni sites of Ni-$TDC_{0.6}BDC_{0.4}$, Ni-BDC, and Ni-TDC. The right region is the bonding orbital, while the left region is the anti-bonding orbital. (g-i) pCOHP between the two H atoms and O atom of the adsorbed H_2O on Ni-$TDC_{0.6}BDC_{0.4}$, Ni-BDC, and Ni-TDC. (j) The △ICOHP values of the two O—H bonds of H_2O on Ni-$TDC_{0.6}BDC_{0.4}$, Ni-BDC, and Ni-TDC. (k) ELF evaluations for H_2O adsorption on the Ni sites of Ni-$TDC_{0.6}BDC_{0.4}$, Ni-BDC, and Ni-TDC. (l) Schematic illustration on the evolution of interfacial water on the Ni-$TDC_{0.6}BDC_{0.4}$, Ni-BDC, and Ni-TDC during OER process.

15213773, 2026, 23, Downloaded from https://onlinelibrary.wiley.com/doi/10.1002/anie.9878440 by Xiulin Yang - South University Of Science , Wiley Online Library on [02/06/2026]. See the Terms and Conditions (https://onlinelibrary.wiley.com/terms-and-conditions) on Wiley Online Library for rules of use; OA articles are governed by the applicable Creative Commons License

the proportion of 4—HB—H_2O in Ni-$TDC_{0.6}BDC_{0.4}$ is lower than that in Ni-BDC and Ni-TDC, while the proportion of K^+—H_2O is significantly higher (Figure 5c). This indicates that the local environment of high-spin state Ni^{3+} in Ni-$TDC_{0.6}BDC_{0.4}$ can promote the reconstruction of interfacial water and the rearrangement of hydrogen-bond network in the electronic double layer (EDL), driving the dynamic transformation of hydrogen-bond water to free-H_2O and forming a continuously enriched free-H_2O environment. Such an environment is conducive to reducing the energy barrier of interfacial water dissociation and ensuring a continuous supply of available reactants [68]. In contrast, the intermediate-spin state Ni^{2+} in Ni-BDC and Ni-TDC, due to its complete coordination and stable electronic state, is difficult to weaken the strong hydrogen bonds of water, resulting in high-energy water dominating the interface and hindering the water activation of OER. Additionally, the vibration frequency of the adsorbate changes with the variation of the electrode potential, which can be attributed to the vibration Stark effect [69]. And the steeper the Stark slope, the higher the sensitivity to the local electric field. As shown in Figure 5d, the Stark slope of K^+—H_2O on Ni-$TDC_{0.6}BDC_{0.4}$ ($-42.5\ cm^{-1}\ V^{-1}$) is significantly steeper than that of 4—HB—H_2O ($-23.4\ cm^{-1}\ V^{-1}$) and 2—HB—H_2O (-30.7 cm^{-1} V^{-1}), indicating that free-H_2O is consumed preferentially during the OER process. More importantly, the Stark slope of K^+—H_2O on Ni-$TDC_{0.6}BDC_{0.4}$ is steeper than that of Ni-BDC and Ni-TDC (Figure S26a,b), manifesting that the free-H_2O is more sensitive to the local electronic environment of the high-spin Ni^{3+}, which is conducive to inducing the dynamic transformation of the rigid hydrogen bond network and enhancing the accumulation of interfacial water on the surface to improve the OER activity.

The mechanism of the effect of electron spin state on the regulation of interface water is further revealed by theoretical calculation. As displayed in Figure 5e, the water adsorption energy of Ni-$TDC_{0.6}BDC_{0.4}$ is -0.682 eV, which is significantly lower than that of Ni-BDC (-0.327 eV) and Ni-TDC (0.278 eV), indicating that Ni-$TDC_{0.6}BDC_{0.4}$ has stronger adsorption capacity for water and is beneficial to the initial adsorption step of water in the OER process. The interaction between the O atom of adsorbed H_2O and Ni sites was analyzed via the projected crystal orbital Hamilton population (pCOHP). As seen in Figure 5f, the number of electrons in the bonding orbitals below the Fermi level increases, while the anti-bonding orbitals shift upward with a reduced electron population in Ni-$TDC_{0.6}BDC_{0.4}$. The Ni-$TDC_{0.6}BDC_{0.4}$ exhibits a more negative integrated COHP (ICOHP) value (-2.49 eV) compared to Ni-BDC (-2.32 eV) and Ni-TDC (-2.48 eV), revealing the strong bonding interaction between the O atom of adsorbed H_2O molecules and the high-spin Ni^{3+} sites on Ni-$TDC_{0.6}BDC_{0.4}$ [70]. Furthermore, the pCOHP of the two O—H bonds in adsorbed H_2O and their integrated COHP difference ($\triangle$ICOHP) on the catalysts were further analyzed (Figure 5g,i). As presented in Figure 5j, Ni-$TDC_{0.6}BDC_{0.4}$ exhibits a more pronounced $\triangle$ICOHP (0.66 eV) compared to Ni-BDC ($\triangle$ICOHP = 0.40 eV) and Ni-TDC ($\triangle$ICOHP = 0.10 eV). This result demonstrates the strongest hydrogen bond dragging force on Ni-$TDC_{0.6}BDC_{0.4}$ and the favorable water adsorption/dissociation kinetics [71]. Electron localization function (ELF) evaluations reveal that Ni-$TDC_{0.6}BDC_{0.4}$ features enhanced electron delocalization at Ni sites and intensified electron localization around the surface H atoms of adsorbed H_2O (Figure 5k). This observation corroborates that high-spin Ni^{3+} facilitates directed electron transfer toward H atoms, exerting a concurrent polarization effect on the strong covalent bonds of H_2O molecules. In summary, the interfacial water evolution mechanisms of the three catalysts in alkaline OER are illustrated in Figure 5l. Ni-$TDC_{0.6}BDC_{0.4}$, endowed with excellent water adsorption capacity and hydrogen bond dragging effect, facilitates the migration of water molecules from the outer Helmholtz plane (OHP) to the inner Helmholtz plane (IHP), forming a free-H_2O-enriched environment. Additionally, oxygen vacancies further accelerate water activation and the OER process. In contrast, Ni-BDC and Ni-TDC exhibit weakened water adsorption and hydrogen bond regulation capabilities, making it difficult to convert high-energy 4—HB/2—HB—H_2O into reaction-favorable free-H_2O, thereby resulting in insufficient free-H_2O supply at active sites.

To probe the potential role of Ni spin-state transition in accelerating OER kinetics, density functional theory (DFT) calculations were performed. The electron distribution at Ni sites was evaluated via the ELF. As demonstrated in Figure 6a, the electrons at high-spin Ni^{3+} sites in Ni-$TDC_{0.6}BDC_{0.4}$ are more delocalized than those in Ni-TDC and Ni-BDC. This facilitates the formation of a continuous spin channel between Ni cations and O anions during OER, thereby promoting charge transfer during the electrocatalytic process [17]. The calculated density of states (DOS) reveals that the d-band center (ε_d = -2.36 eV) of Ni-$TDC_{0.6}BDC_{0.4}$ is closer to the Fermi level (E_f) than that of Ni-TDC (ε_d = -2.95 eV) and Ni-BDC (ε_d = -2.50 eV) (Figure 6b). This indicates that the d-band center of the active Ni sites in Ni-$TDC_{0.6}BDC_{0.4}$ is shifted upward, which enhances the adsorption capacity for oxygen-containing intermediates and thereby accelerates the OER kinetics [14, 72]. Furthermore, the projected DOS (PDOS) analysis was conducted after OH^- adsorption on Ni sites. As depicted in Figure 6c, the Ni 3d orbitals in Ni-$TDC_{0.6}BDC_{0.4}$ exhibit greater overlap with the O 2p orbitals of adsorbed OH^- near the E_f, compared to Ni-TDC and Ni-BDC, signifying the stronger 3d-2p hybridization between high-spin Ni^{3+} sites and adsorbed OH^- [10]. The adsorption strength of OH^- on Ni sites was further investigated via COHP calculations (Figure 6d). Compared to Ni-TDC and Ni-BDC, the anti-bonding orbital in Ni-$TDC_{0.6}BDC_{0.4}$ is elevated above the E_f, indicating that the anti-bonding orbital is not filled with electrons, thereby strengthening the bonding. Additionally, the ICOHP is calculated to quantitatively evaluate the bonding strength. As seen in Figure 6e, the ICOHP value of Ni-$TDC_{0.6}BDC_{0.4}$ (-5.17 eV) is more negative than that of Ni-TDC (-4.39 eV) and Ni-BDC (-4.60 eV), confirming the presence of a stronger Ni—OH bond between Ni-$TDC_{0.6}BDC_{0.4}$ and OH^- [73]. The potential orbital interactions between adsorbed OH^- and Ni sites were described using bond order theory. Based on symmetry conservation principles, the $d_{x^2-y^2}$ and d_{x-y} orbitals do not interact with OH^- orbitals [50]. To quantitatively evaluate bond strength, the bond order is calculated using the formula: Bond order = (A-B)/2, where *A* and *B* represent bonding electrons and anti-bonding electrons, respectively. As shown in Figures 6f,g, the bond order between Ni-$TDC_{0.6}BDC_{0.4}$ and OH^- (1.0) is greater than that of Ni-TDC and Ni-BDC (0.5), further demonstrating that the high-spin Ni^{3+} ions have a stronger adsorption of OH^- ions. This is attributed to the magnetic properties of Ni-$TDC_{0.6}BDC_{0.4}$ and the spin polarization of Ni electrons generating an inhomogeneous relaxation field that facilitates the adsorption of OH^- ions during the reaction process [17, 74]. Based on the four-electron transfer mechanism

15213773, 2026, 23, Downloaded from https://onlinelibrary.wiley.com/doi/10.1002/anie.9878440 by Xinlin Yang - South University Of Science , Wiley Online Library on [02/06/2026]. See the Terms and Conditions (https://onlinelibrary.wiley.com/terms-and-conditions) on Wiley Online Library for rules of use; OA articles are governed by the applicable Creative Commons License

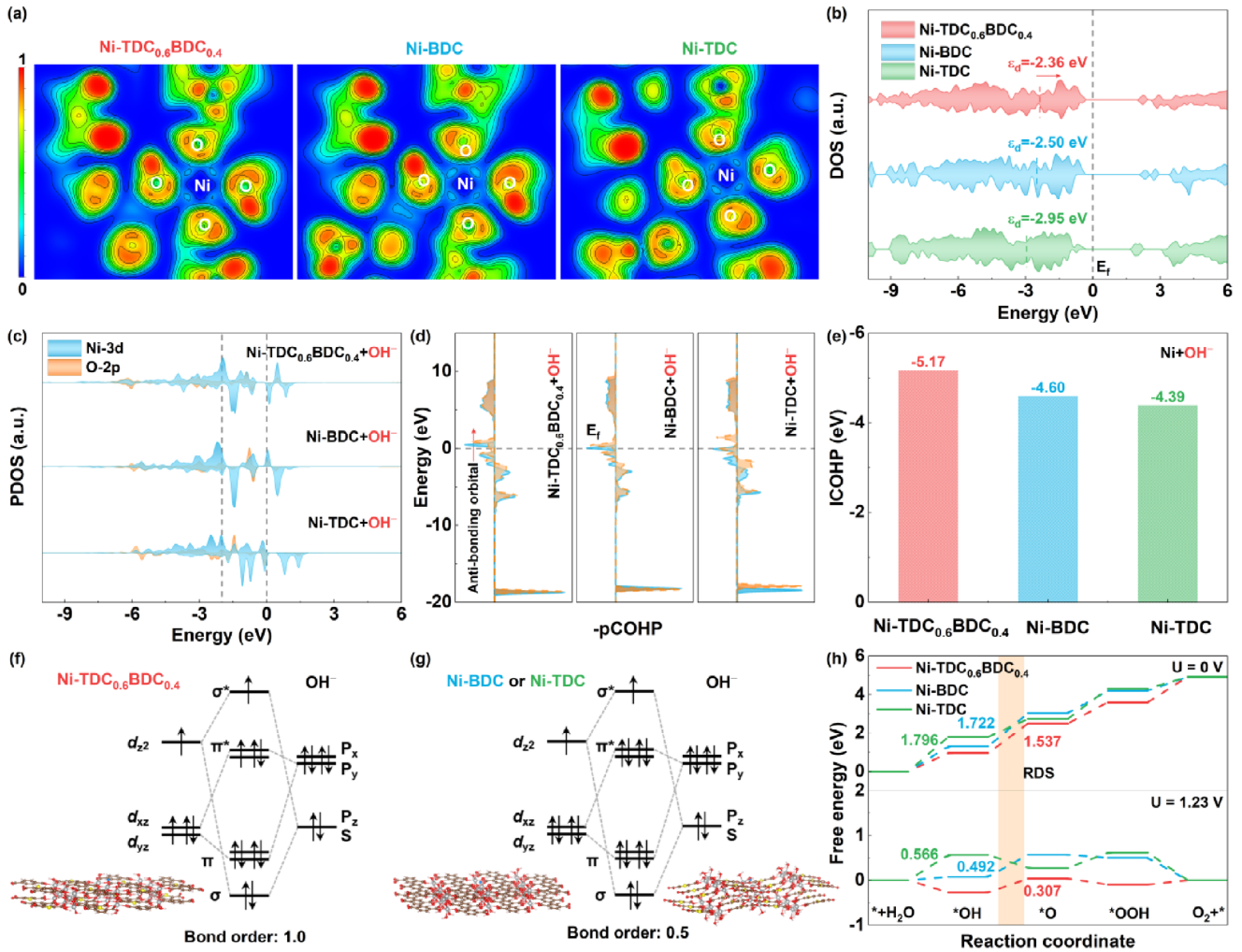

FIGURE 6 | Density functional theory calculation analysis. (a) ELF evaluations. Blue represents delocalized electrons (0), while red represents localized electrons (1). (b) The calculated DOS. (c) The calculated PDOS when OH^- ions are adsorbed on the Ni sites. (d) COHP of Ni—OH bond for OH^- ions adsorbed on the Ni sites. The right region is the bonding orbital, while the left region is the anti-bonding orbital. (e) ICOHP between adsorbed OH^- ions and Ni sites. (f) The orbital interactions between Ni-$TDC_{0.6}BDC_{0.4}$ and OH^- ions. (g) The orbital interactions between Ni-TDC (or Ni-BDC) and OH^- ions. (h) OER Gibbs free energy diagram.

under alkaline conditions, the optimal models for the reaction intermediates of Ni-TDC0.6BDC0.4, Ni-TDC, and Ni-BDC during the OER process were established (Figures S27–S29). To elucidate the structure-activity relationship between Ni spin states and catalytic activity, the Gibbs free energy (ΔG) of each elementary OER step was calculated. Typically, the step with the largest ΔG is identified as the rate-determining step (RDS), which dictates the theoretical overpotential [75]. As shown in Figure 6h, at U = 0 V, the RDS of Ni-TDC0.6BDC0.4 and Ni-BDC corresponds to the *OH→*O conversion, while that of Ni-TDC corresponds to *OH adsorption. Notably, the ΔG_{RDS} for Ni-TDC0.6BDC0.4 (1.537 eV) is much lower than that of Ni-BDC (1.722 eV) and Ni-TDC (1.796 eV). Intriguingly, Ni-TDC0.6BDC0.4 exhibits a lower energy barrier for *OH adsorption that is the initial OER step. This can be ascribed to the increased hole states in the t_{2g} orbitals of high-spin Ni^{3+} sites, which enhance the electrophilicity of adsorbed O and promote the adsorption of oxygen-containing intermediates [76]. At U = 1.23 V, the total free energy of Ni-$TDC_{0.6}BDC_{0.4}$ drops below zero, indicating an exothermic and spontaneous reaction. More importantly, Ni-$TDC_{0.6}BDC_{0.4}$ demonstrates reduced values for both ΔG_{RDS} and ΔG (*OOH→O_2) compared to Ni-BDC and Ni-TDC. Thus, the high-spin Ni^{3+} sites in Ni-$TDC_{0.6}BDC_{0.4}$ not only facilitate the adsorption of oxygen-containing intermediates and oxygen release, but also reduce the energy barrier of RDS, thereby accelerating OER kinetics and enhancing OER activity.

Benefiting from the excellent OER performance of Ni-$TDC_{0.6}BDC_{0.4}$, we assembled an anion exchange membrane water electrolyzer (AEMWE) using Ni-$TDC_{0.6}BDC_{0.4}$ as the anode and commercial Pt/C as the cathode to evaluate its potential for practical industrial applications (Figure 7a) As presented in Figure 7b,c, the Ni-$TDC_{0.6}BDC_{0.4}{}^{(+)}$ || $Pt/C^{(-)}$ electrolyzer only requires cell voltages of 2.40 and 2.07 V to achieve a current density of 1.5 A cm^{-2} at 25 and 60°C, respectively, outperforming the $RuO_2{}^{(+)}$ || $Pt/C^{(-)}$ electrolyzer (2.46 V@25°C and 2.13 V@60°C). More importantly, the Ni-$TDC_{0.6}BDC_{0.4}{}^{(+)}$ || $Pt/C^{(-)}$ electrolyzer exhibits higher activity at higher current densities (greater than 1.5 A cm^{-2}). Furthermore, the AEMWE performance of Ni-$TDC_{0.6}BDC_{0.4}$-based electrolyzer surpasses that of most previously reported AEMWE systems (Figure 7d,e,

15213773, 2026, 23, Downloaded from https://onlinelibrary.wiley.com/doi/10.1002/anie.9878440 by Xiulin Yang - South University Of Science , Wiley Online Library on [02/06/2026]. See the Terms and Conditions (https://onlinelibrary.wiley.com/terms-and-conditions) on Wiley Online Library for rules of use; OA articles are governed by the applicable Creative Commons License

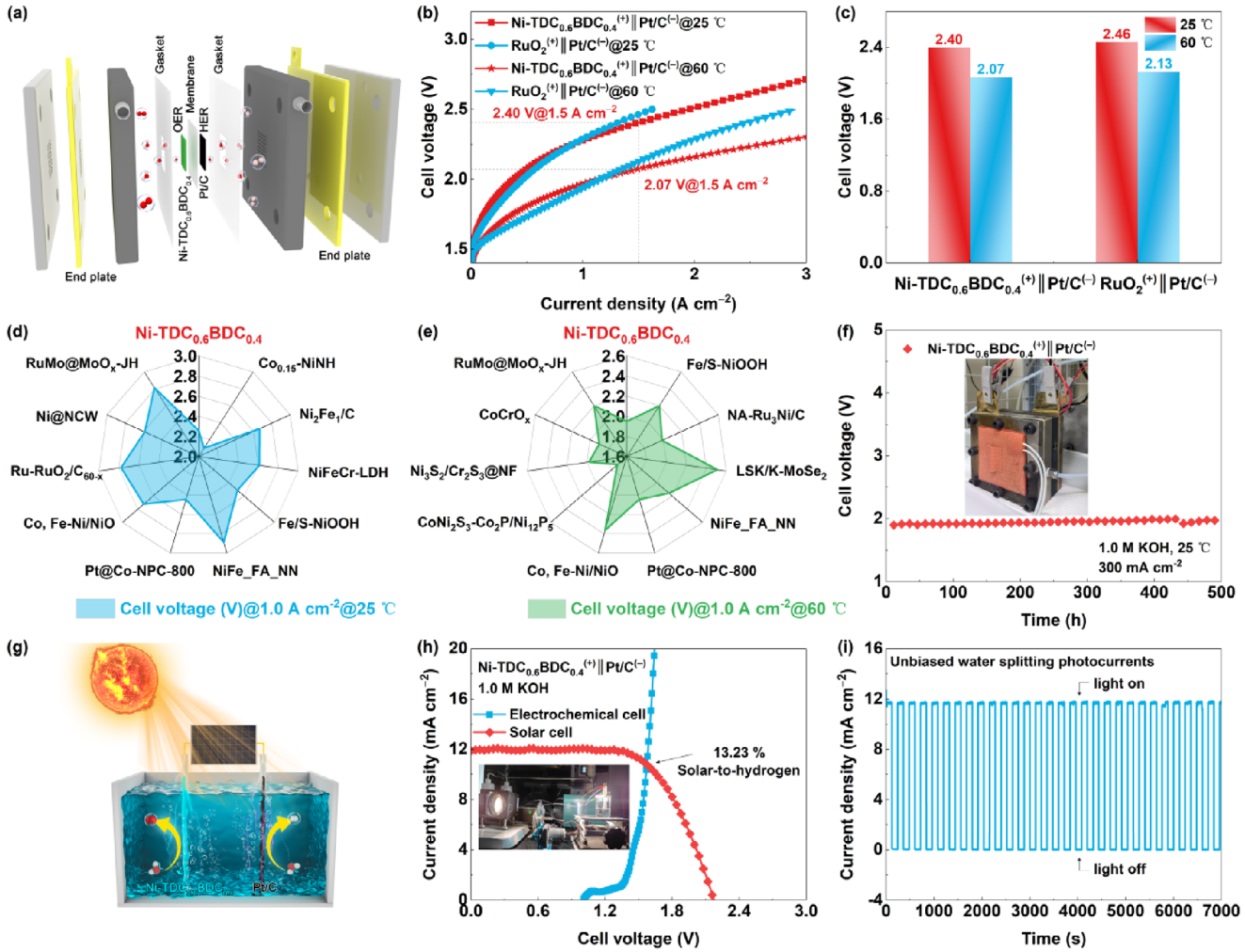

FIGURE 7 | Electrochemical performance of AEMWE device and photovoltaic-driven OWS in 1.0 M KOH solution. (a) Schematic diagram of the AEMWE device. (b) Polarization curves. (c) Comparison of the cell voltage at 25 and 60°C. Comparison with the reported performance of AEMWE devices (d) at 25°C and (e) at 60°C. (f) Stability measurements at 300 mA cm^{-2}. (g) Schematic diagram of the photovoltaic-driven OWS device under solar irradiation. (h) The current-voltage curve of the photovoltaic device under AM 1.5 G illumination. (i) Time-dependent current output from photovoltaic without external bias.

and Table S6). Meanwhile, the long-term stability of the as-assembled AEMWE was evaluated via the chronopotentiometry testing. As shown in Figure 7f, the AEMWE system demonstrates exceptional stability, operating continuously for 500 h at 300 mA cm^{-2} without any noticeable potential degradation. Additionally, we integrated the Ni-TDC$_{0.6}$BDC$_{0.4}$$^{(+)}$ || Pt/C$^{(-)}$ two-electrode system with a commercial solar panel to construct a bias-free solar-driven alkaline OWS system (Figure 7f) [77]. The current-voltage (J-V) characteristic curves reveal that the solar-driven electrolyzer achieves a solar-to-hydrogen (STH) efficiency of 13.23% (Figure 7g). Moreover, the operational stability of this photovoltaic-electrolysis device was assessed. As illustrated in Figure 7i, under intermittent illumination with 60 s on/off cycles, the solar-driven current output of the system displays no substantial degradation or fluctuation during a continuous 7000 s test, confirming the viability of the solar-driven OWS technology based on the Ni-TDC$_{0.6}$BDC$_{0.4}$ electrode. Therefore, photovoltaic-driven OWS device with high STH conversion efficiency, coupled with outstanding industrial-grade current output capability and stability, provide feasible conditions for the Ni-TDC$_{0.6}$BDC$_{0.4}$ catalyst to achieve green hydrogen production.

3 | Conclusion

In summary, this study establishes that a dual-ligand coordination strategy can be harnessed to manipulate the atomic-scale geometry of Ni sites within MOFs, inducing lattice expansion and creating a defective local environment rich in oxygen vacancies and coordinatively unsaturated sites. These structural perturbations directly drive the critical electronic transition of Ni from an intermediate-spin (Ni^{2+}) to a high-spin (Ni^{3+}) state. This targeted spin-state engineering concurrently enhances the intrinsic adsorption of reaction intermediates and favorably restructures the interfacial water network, collectively breaking the OER kinetics bottleneck. The Ni-TDC$_{0.6}$BDC$_{0.4}$ catalyst exhibits superior OER activity, achieving a low overpotential of 230 mV at 10 mA cm^{-2}, a small Tafel slope of 53.3 mV dec^{-1}. Additionally, the assembled The Ni-TDC$_{0.6}$BDC$_{0.4}$-based

15213773, 2026, 23, Downloaded from https://onlinelibrary.wiley.com/doi/10.1002/anie.9878440 by Xinlin Yang - South University Of Science , Wiley Online Library on [02/06/2026]. See the Terms and Conditions (https://onlinelibrary.wiley.com/terms-and-conditions) on Wiley Online Library for rules of use; OA articles are governed by the applicable Creative Commons License

AEMWE exhibits superior performance with low cell voltages of 2.04 (25°C) and 2.07 V (60°C) at 1.5 A cm^{-2}, operating stably 500 h at 300 mA cm^{-2}. And its solar-driven OWS device achieves 13.23% STH efficiency. This work highlights the significance of electronic spin states optimization in enhancing OER activity and offers a viable strategy for developing advanced electrocatalysts for sustainable energy applications.

Acknowledgments

This work has been supported by the National Natural Science Foundation of China (no. 52363028, 21965005, 52025013, 22121005), the Guangxi Technology Base and Talent Subject (GUIKE AD23023004, GUIKE AD20297039), the innovation project of Guangxi Graduate Education (YCBZ2025097), the National Research Foundation, Singapore, and A*STAR (Agency for Science, Technology and Research) under its LCER Phase 2 programme first emerging technology (Award No. U2411D4006), Key Laboratory of Functional Inorganic Material Chemistry, Heilongjiang University, Ministry of Education, P. R. China (Award No. KIM-K-2025001) and Key Laboratory of Applied Surface and Colloid Chemistry (Shaanxi Normal University), Ministry of Education, P. R. China (Award No. 2025072).

Conflicts of Interest

The authors declare no competing interest.

Data Availability Statement

The data that support the findings of this study are available from the corresponding author upon reasonable request.

References

1. Q. Kang, M. Su, Y. Luo, T. Wang, F. Gao, and Q. Lu, "Chemical Fermentation PoreCreation on Multilevel Bio-Carbon Structure With in Situ Ni–Fe Alloy Loading for Superior Oxygen Evolution Reaction Electrocatalysis," *Nano-Micro Lett* 17 (2025): 269, https://doi.org/10.1007/s40820-025-01777-2.

2. L. Peng, C. Wang, Q. Wang, R. Shi, T. Zhang, and G. I. N. Waterhouse, "Rationally Designed Ni–Ni_3S_2 Interfaces for Efficient Overall Water Electrolysis," *Adv Energy Sustain Res* 2 (2021): 2100078, https://doi.org/10.1002/aesr.202100078.

3. C.-H. Li, C.-Z. Yuan, X. Huang, et al., "Tailoring the Electron Redistribution of RuO_2 by Constructing a Ru-O-La Asymmetric Configuration for Efficient Acidic Oxygen Evolution," *eScience* 5 (2025): 100307, https://doi.org/10.1016/j.esci.2024.100307.

4. W. Peng, A. Deshmukh, N. Chen, et al., "Deciphering the Dynamic Structure Evolution of Fe- and Ni-Codoped CoS_2 for Enhanced Water Oxidation," *ACS Catal* 12 (2022): 3743–3751, https://doi.org/10.1021/acscatal.2c00328.

5. Z. Hu, H. Wu, X. Yong, et al., "Advances in Dual-Site Mechanisms for Designing High-Performance Oxygen Evolution Electrocatalysts," *eScience* 5 (2025): 100403, https://doi.org/10.1016/j.esci.2025.100403.

6. Y. Zhang, T. Wang, L. Mei, et al., "Rational Design of Cost-Effective Metal-Doped ZrO_2 for Oxygen Evolution Reaction," *Nano-Micro Lett* 16 (2024): 180, https://doi.org/10.1007/s40820-024-01403-7.

7. G. Lin, A. Dong, Z. Li, et al., "An Interlayer Anchored NiMo/MoO_2 Electrocatalyst for Hydrogen Evolution Reaction in Anion Exchange Membrane Water Electrolysis at High Current Density," *Advanced Materials* 37 (2025): 2507525, https://doi.org/10.1002/adma.202507525.

8. Z. Su, Q. Huang, Q. Guo, S. J. Hoseini, F. Zheng, and W. Chen, "Metal–Organic Framework and Carbon Hybrid Nanostructures: Fabrication Strategies and Electrocatalytic Application for the Water Splitting and Oxygen Reduction Reaction," *Nano Research Energy* 2 (2023): e9120078.

9. Z. Li, X. Wu, X. Jiang, et al., "Surface Carbon Layer Controllable Ni_3Fe Particles Confined in Hierarchical N-Doped Carbon Framework Boosting Oxygen Evolution Reaction," *Adv Powder Mater* 1 (2022): 100020, https://doi.org/10.1016/j.apmate.2021.11.007.

10. X. Ren, T. Wu, Y. Sun, et al., "Spin-Polarized Oxygen Evolution Reaction Under Magnetic Field," *Nature Communications* 12 (2021): 2608, https://doi.org/10.1038/s41467-021-22865-y.

11. Z. Fang, W. Zhao, T. Shen, et al., "Spin-Modulated Oxygen Electrocatalysis," *Precis Chem* 1 (2023): 395–417, https://doi.org/10.1021/prechem.3c00059.

12. M. Li, J. Yang, S. Li, et al., "Rare-Earth-Induced Intermediate-Spin Co Centers in $MnCo_2$ $O_{4.5}$ for Sustainable Acidic Water Oxidation," *Journal of the American Chemical Society* 147 (2025): 45680–45690, https://doi.org/10.1021/jacs.5c17361.

13. Y. Long, S. Zhao, L. Wang, et al., "Regulating High Electron Spin State in Co_3S_4 for Enhanced Water Splitting," *ACS Catal* 15 (2025): 9845–9855, https://doi.org/10.1021/acscatal.4c07849.

14. W. Zhong, Z. Li, Q. Sun, et al., "Spin Modulation of Antiperovskite Nitride for Industrial-Current-Density Seawater Electrolysis," *ACS Nano* 20 (2026): 3476–3486, https://doi.org/10.1021/acsnano.5c13813.

15. Z.-D. He, R. Tesch, M. J. Eslamibidgoli, M. H. Eikerling, and P. M. Kowalski, "Low-Spin State of Fe in Fe-doped NiOOH Electrocatalysts," *Nature Communications* 14 (2023): 3498, https://doi.org/10.1038/s41467-023-38978-5.

16. M. Lu, Y. Du, S. Yan, T. Yu, and Z. Zou, "Thermally Stimulated Spin Switching Accelerates Water Electrolysis," *Physical Review Letter* 133 (2024): 258001, https://doi.org/10.1103/PhysRevLett.133.258001.

17. Z. Du, Z. Meng, X. Gong, et al., "Rapid Surface Reconstruction of Pentlandite by High-Spin State Iron for Efficient Oxygen Evolution Reaction," *Angewandte Chemie International Edition* 63 (2024): e202317022, https://doi.org/10.1002/anie.202317022.

18. L. Yang, R. He, M. Botifoll, et al., "Enhanced Oxygen Evolution and Zinc-Air Battery Performance via Electronic Spin Modulation in Heterostructured Catalysts," *Advanced Materials* 36 (2024): 2400572, https://doi.org/10.1002/adma.202400572.

19. L. Wu, W. Huang, D. Li, et al., "Unveiling the Structure and Dissociation of Interfacial Water on RuO_2 for Efficient Acidic Oxygen Evolution Reaction," *Angewandte Chemie International Edition* 64 (2025): e202413334, https://doi.org/10.1002/anie.202413334.

20. S. Zhu, R. Yang, H. J. W. Li, et al., "Reconstructing Hydrogen-Bond Network for Efficient Acidic Oxygen Evolution," *Angewandte Chemie International Edition* 63 (2024): e202319462, https://doi.org/10.1002/anie.202319462.

21. W.-G. Cui, X. Ren, S. Wang, et al., "Modulating the Structure of Interfacial Water via Oxygen-Coordinated Tungsten Single-Atom on Nickel Sulfide Slab to Boost Alkaline Hydrogen Evolution," *Advanced Energy Materials* 15 (2025): e03257, https://doi.org/10.1002/aenm.202503257.

22. J. Ma, C. Qiu, J. J. Wang, et al., "Spin-State Engineering of Co^{3+} for Optimized Interfacial Microenvironment and Enhanced Glycerol Electrooxidation," *Advanced Functional Materials* 35 (2025): e22517.

23. Z. Fang, B. Bueken, D. E. De Vos, and R. A. Fischer, "Defect-Engineered Metal–Organic Frameworks," *Angewandte Chemie International Edition* 54 (2015): 7234–7254, https://doi.org/10.1002/anie.201411540.

24. A. Carton, A. Mesbah, T. Mazet, F. Porcher, and M. François, "Ab Initio Crystal Structure of Nickel(II) Hydroxy-Terephthalate by Synchrotron Powder Diffraction and Magnetic Study," *Solid State Sciences* 9 (2007): 465–471, https://doi.org/10.1016/j.solidstatesciences.2007.04.003.

25. A. Demessence, A. Mesbah, M. François, G. Rogez, and P. Rabu, "Structure and Magnetic Properties of a New 1D Nickel(II) Hydrox-

15213773, 2026, 23, Downloaded from https://onlinelibrary.wiley.com/doi/10.1002/anie.9878440 by Xinlin Yang - South University Of Science , Wiley Online Library on [02/06/2026]. See the Terms and Conditions (https://onlinelibrary.wiley.com/terms-and-conditions) on Wiley Online Library for rules of use; OA articles are governed by the applicable Creative Commons License

ythiophenedicarboxylate," *European Journal of Inorganic Chemistry* 2009 (2009): 3713–3720, https://doi.org/10.1002/ejic.200900329.

26. K. Metavarayuth, O. Ejegbavwo, G. McCarver, et al., "Direct Identification of Mixed-Metal Centers in Metal–Organic Frameworks: Cu_3 (BTC) 2 Transmetalated With Rh^{2+} Ions," *Journal of Physical Chemistry Letters* 11 (2020): 8138–8144, https://doi.org/10.1021/acs.jpclett.0c02539.

27. V. V. Butova, A. P. Budnyk, K. M. Charykov, et al., "Partial and Complete Substitution of the 1,4-Benzenedicarboxylate Linker in UiO-66 With 1,4-Naphthalenedicarboxylate: Synthesis, Characterization, and H_2 -Adsorption Properties," *Inorganic Chemistry* 58 (2019): 1607–1620, https://doi.org/10.1021/acs.inorgchem.8b03087.

28. J. Huang, H. Sheng, R. D. Ross, et al., "Modifying Redox Properties and Local Bonding of Co_3O_4 by CeO_2 Enhances Oxygen Evolution Catalysis in Acid," *Nature Communications* 12 (2021): 3036, https://doi.org/10.1038/s41467-021-23390-8.

29. Y. Sun, K. Xu, Z. Wei, et al., "Strong Electronic Interaction in Dual-Cation-Incorporated $NiSe_2$ Nanosheets With Lattice Distortion for Highly Efficient Overall Water Splitting," *Advanced Materials* 30 (2018): 1802121, https://doi.org/10.1002/adma.201802121.

30. L. Zhong, X. Liao, H. Cui, H. Luo, Y. Lv, and P. Liu, "Hydrogenation of α,β-unsaturated Aldehydes over Defective UiO-66 With Frustrated Lewis Pairs: Modulation of Densities of Defect Sites via Tailoring Ligand-vacancies," *Appl Catal B Environ* 342 (2024): 123421, https://doi.org/10.1016/j.apcatb.2023.123421.

31. K. Yu, H. Yang, H. Zhang, et al., "Immobilization of Oxyanions on the Reconstructed Heterostructure Evolved From a Bimetallic Oxysulfide for the Promotion of Oxygen Evolution Reaction," *Nano-Micro Lett* 15 (2023): 186, https://doi.org/10.1007/s40820-023-01164-9.

32. Y. Liu, Y. Chen, Y. Tian, et al., "Synergizing Hydrogen Spillover and Deprotonation by the Internal Polarization Field in a MoS_2 /$NiPS_3$ Vertical Heterostructure for Boosted Water Electrolysis," *Advanced Materials* 34 (2022): 2203615, https://doi.org/10.1002/adma.202203615.

33. Q. Hong, Y. Wang, R. Wang, et al., "In Situ Coupling of Carbon Dots With Co-ZIF Nanoarrays Enabling Highly Efficient Oxygen Evolution Electrocatalysis," *Small* 19 (2023): 2206723, https://doi.org/10.1002/smll.202206723.

34. Y. Sun, Y. Li, L. Dai, et al., "An Unconventional Seawater Acceleration Effect Enables High-Spin Cobalt Sites for Industrial-Level Seawater Electrooxidation," *Advanced Functional Materials* 35 (2025): 2419626, https://doi.org/10.1002/adfm.202419626.

35. D. R. Paudel, U. N. Pan, R. B. Ghising, et al., "Multi-interfacial Dendritic Engineering Facilitating Congruous Intrinsic Activity of Oxide-carbide/MOF Nanostructured Multimodal Electrocatalyst for Hydrogen and Oxygen Electrocatalysis," *Appl Catal B Environ* 331 (2023): 122711.

36. W. Zhai, Y. Chen, Y. Liu, et al., "Covalently Bonded Ni Sites in Black Phosphorene With Electron Redistribution for Efficient Metal-Lightweighted Water Electrolysis," *Nano-Micro Lett* 16 (2024): 115, https://doi.org/10.1007/s40820-024-01331-6.

37. H. Xu, D. J. Zheng, S. Wang, et al., "Stable Metal–Organic Electrocatalysts for Anion-Exchange Membrane Water Electrolyzers by Defect Engineering," *Journal of the American Chemical Society* 147 (2025): 29838–29851, https://doi.org/10.1021/jacs.5c06156.

38. X. Zhang, Y. Zhao, R. Shi, G. I. N. Waterhouse, and T. Zhang, "A Simple Synthetic Strategy Toward Defect-Rich Porous Monolayer NiFe-Layered Double Hydroxide Nanosheets for Efficient Electrocatalytic Water Oxidation," *Advanced Energy Materials* 9 (2019): 1900881, https://doi.org/10.1002/aenm.201900881.

39. G. Zhuang, Y. Chen, Z. Zhuang, Y. Yu, and J. Yu, "Oxygen Vacancies in Metal Oxides: Recent Progress towards Advanced Catalyst Design," *Sci China Mater* 63 (2020): 2089–2118, https://doi.org/10.1007/s40843-020-1305-6.

40. H. Qin, J. Li, G. Lin, et al., "Tuning Surface Coordination Environment of Ni_3 N by Fluorine Modification for Efficient Methanol Electrooxidation Assisted Hydrogen Evolution," *Advanced Materials* 37 (2025): 2507573, https://doi.org/10.1002/adma.202507573.

41. H. Qin, G. Lin, J. Zhang, et al., "Enhanced Cooperative Generalized Compressive Strain and Electronic Structure Engineering in W-Ni_3N for Efficient Hydrazine Oxidation Facilitating H_2 Production," *Advanced Materials* 37 (2025): 2417593, https://doi.org/10.1002/adma.202417593.

42. J.-Y. Zhang, Y. Yan, B. Mei, et al., "Local Spin-State Tuning of Cobalt–Iron Selenide Nanoframes for the Boosted Oxygen Evolution," *Energy & Environmental Science* 14 (2021): 365–373, https://doi.org/10.1039/D0EE03500A.

43. X. Wang, S. Xi, P. Huang, et al., "Pivotal Role of Reversible NiO_6 Geometric Conversion in Oxygen Evolution," *Nature* 611 (2022): 702–708, https://doi.org/10.1038/s41586-022-05296-7.

44. J. Ding, D. Guo, N. Wang, et al., "Defect Engineered Metal–organic Framework With Accelerated Structural Transformation for Efficient Oxygen Evolution Reaction," *Angewandte Chemie International Edition* 62 (2023): e202311909.

45. Y. Zhao, X. Jia, G. Chen, et al., "Ultrafine NiO Nanosheets Stabilized by TiO_2 From Monolayer NiTi-LDH Precursors: An Active Water Oxidation Electrocatalyst," *Journal of the American Chemical Society* 138 (2016): 6517–6524, https://doi.org/10.1021/jacs.6b01606.

46. H. Zhong, Q. Zhang, J. Yu, et al., "Key Role of e_g* Band Broadening in Nickel-Based Oxyhydroxides on Coupled Oxygen Evolution Mechanism," *Nature Communications* 14 (2023): 7488, https://doi.org/10.1038/s41467-023-43302-2.

47. X. Wang, Z. Xiong, S. Yang, et al., "Proximity Engineering of Fe–N_4 Twins for Oriented Generation of Singlet Oxygen for Hospital Wastewater Treatment," *Angewandte Chemie International Edition* 65 (2026): e6249880, https://doi.org/10.1002/anie.6249880.

48. Y. Liu, L. Li, X. Li, et al., "Asymmetric Tacticity Navigates the Localized Metal Spin State for Sustainable Alkaline/Sea Water Oxidation," *Science Advances* 11 (2025): eads0861.

49. Y. Zhang, H. Ullah, L. Li, et al., "Leveraging Co Spin State in Metal–Organic Frameworks for Efficient Water Oxidation," *ACS Catal* 15 (2025): 17155–17165, https://doi.org/10.1021/acscatal.5c03901.

50. Z.-Y. Mei, G. Zhao, C. Xia, et al., "Regulated High-Spin State and Constrained Charge Behavior of Active Cobalt Sites in Covalent Organic Frameworks for Promoting Electrocatalytic Oxygen Reduction," *Angewandte Chemie International Edition* 62 (2023): e202303871, https://doi.org/10.1002/anie.202303871.

51. K. Zhu, X. Zhu, and W. Yang, "Application of in Situ Techniques for the Characterization of NiFe-Based Oxygen Evolution Reaction (OER) Electrocatalysts," *Angewandte Chemie International Edition* 58 (2019): 1252–1265, https://doi.org/10.1002/anie.201802923.

52. G. Lin, H. Qin, X. Cao, F. Cheng, L. Jiao, and J. Chen, "Regulation of Relay Catalytic Mechanism for Efficient Methanol Oxidation Reaction," *Angewandte Chemie International Edition* 64 (2025): e202506215.

53. S. Lee, Y.-C. Chu, L. Bai, H. M. Chen, and X. Hu, "Operando Identification of a Side-on Nickel Superoxide Intermediate and the Mechanism of Oxygen Evolution on Nickel Oxyhydroxide," *Chem Catalysis* 3 (2023): 100475, https://doi.org/10.1016/j.checat.2022.11.014.

54. Y. Li, Y. Wu, M. Yuan, et al., "Operando Spectroscopies Unveil Interfacial FeOOH Induced Highly Reactive β-Ni(Fe)OOH for Efficient Oxygen Evolution," *Appl Catal B Environ* 318 (2022): 121825, https://doi.org/10.1016/j.apcatb.2022.121825.

55. X. Bo, R. K. Hocking, S. Zhou, et al., "Capturing the Active Sites of Multimetallic (oxy)Hydroxides for the Oxygen Evolution Reaction," *Energy & Environmental Science* 13 (2020): 4225–4237, https://doi.org/10.1039/D0EE01609H.

56. M. W. Louie and A. T. Bell, "An Investigation of Thin-Film Ni–Fe Oxide Catalysts for the Electrochemical Evolution of Oxygen," *Journal of the American Chemical Society* 135 (2013): 12329–12337, https://doi.org/10.1021/ja405351s.

15213773, 2026, 23, Downloaded from https://onlinelibrary.wiley.com/doi/10.1002/anie.9878440 by Xiulin Yang - South University Of Science , Wiley Online Library on [02/06/2026]. See the Terms and Conditions (https://onlinelibrary.wiley.com/terms-and-conditions) on Wiley Online Library for rules of use; OA articles are governed by the applicable Creative Commons License

57. L. Trotochaud, S. L. Young, J. K. Ranney, and S. W. Boettcher, "Nickel–Iron Oxyhydroxide Oxygen-Evolution Electrocatalysts: The Role of Intentional and Incidental Iron Incorporation," *Journal of the American Chemical Society* 136 (2014): 6744–6753, https://doi.org/10.1021/ja502379c.

58. Y. Shen, X.-L. Zhang, M.-R. Qu, et al., "Cr Dopant Mediates Hydroxyl Spillover on RuO_2 for High-Efficiency Proton Exchange Membrane Electrolysis," *Nature Communications* 15 (2024): 7861, https://doi.org/10.1038/s41467-024-51871-z.

59. Z. Xie, H. Chen, X. Wang, et al., *Angewandte Chemie International Edition* 63 (2024): e202415032.

60. J. Xu, H. Jin, T. Lu, et al., "IrO_x nH_2O With Lattice Water–Assisted Oxygen Exchange for High-Performance Proton Exchange Membrane Water Electrolyzers," *Science Advances* 9 (2023): eadh1718.

61. F. Hu, D. Yu, W.-J. Zeng, et al., "Active Site Tailoring of Metal-Organic Frameworks for Highly Efficient Oxygen Evolution," *Advanced Energy Materials* 13 (2023): 2301224, https://doi.org/10.1002/aenm.202301224.

62. Z. Xiao, Y.-C. Huang, C.-L. Dong, et al., "Operando Identification of the Dynamic Behavior of Oxygen Vacancy-Rich Co_3O_4 for Oxygen Evolution Reaction," *Journal of the American Chemical Society* 142 (2020): 12087–12095, https://doi.org/10.1021/jacs.0c00257.

63. R. Jena, V. Kashyap, R. Jana, et al., "In Situ Tracking of Ni-MOF Reconstruction into Active $Ni(OH)_2$ OER Catalysts," *Angewandte Chemie International Edition* 64 (2025): e202510741, https://doi.org/10.1002/anie.202510741.

64. Y. Wu, Y. Li, M. Yuan, et al., "Operando Capturing of Surface Self-Reconstruction of Ni_3S_2/$FeNi_2S_4$ Hybrid Nanosheet Array for Overall Water Splitting," *Chemical Engineering Journal* 427 (2022): 131944, https://doi.org/10.1016/j.cej.2021.131944.

65. M. Görlin, P. Chernev, J. Ferreira de Araújo, et al., "Oxygen Evolution Reaction Dynamics, Faradaic Charge Efficiency, and the Active Metal Redox States of Ni–Fe Oxide Water Splitting Electrocatalysts," *Journal of the American Chemical Society* 138 (2016): 5603–5614.

66. G. Hai, X. Jia, K. Zhang, X. Liu, Z. Wu, and G. Wang, "High-Performance Oxygen Evolution Catalyst Using Two-Dimensional Ultrathin Metal-Organic Frameworks Nanosheets," *Nano Energy* 44 (2018): 345–352, https://doi.org/10.1016/j.nanoen.2017.11.071.

67. Y. Chen, J. Wang, Z. Yu, et al., "Functional Group Scission-Induced Lattice Strain in Chiral Macromolecular Metal-Organic Framework Arrays for Electrocatalytic Overall Water Splitting," *Appl Catal B Environ* 307 (2022): 121151, https://doi.org/10.1016/j.apcatb.2022.121151.

68. L. Wu, W. Huang, D. Li, B. Zhao, H. Zhou, and W. Luo, "Role of Interfacial Water in Improving the Activity and Stability of Lattice-Oxygen-Mediated Acidic Oxygen Evolution on RuO_2," *Angewandte Chemie International Edition* 64 (2025): e202420848.

69. L. Deng, H. Chen, S.-F. Hung, et al., "Lewis Acid-Mediated Interfacial Water Supply for Sustainable Proton Exchange Membrane Water Electrolysis," *Journal of the American Chemical Society* 146 (2024): 35438–35448, https://doi.org/10.1021/jacs.4c14529.

70. Y. Wan, Y. Tang, Y. Zuo, et al., "Interfacial Hydrogen-Bond Modulation of Dynamic Catalysts for Nitrate Electroreduction to Ammonia," *Energy & Environmental Science* 18 (2025): 7460–7469, https://doi.org/10.1039/D5EE00597C.

71. Q. Wen, J. Duan, W. Wang, et al., "Engineering a Local Free Water Enriched Microenvironment for Surpassing Platinum Hydrogen Evolution Activity," *Angewandte Chemie International Edition* 61 (2022): e202206077, https://doi.org/10.1002/anie.202206077.

72. S. Yang, X. Liu, X. Wang, et al., "High-Entropy Type Fe-Ni-P-O-C Amorphous Nanospheres: Remarkable Fe-ion Migration Induced Efficient Surface Reconstruction for Oxygen Evolution Reaction," *Adv Powder Mater* 4 (2025): 100329, https://doi.org/10.1016/j.apmate.2025.100329.

73. J. Qiao, C. Lu, L. Kong, et al., "Spin Engineering of Fe—N—C by Axial Ligand Modulation for Enhanced Bifunctional Oxygen Catalysis," *Advanced Functional Materials* 34 (2024): 2409794, https://doi.org/10.1002/adfm.202409794.

74. R. Chen, Z. Zhang, Z. Wang, et al., "Constructing Air-Stable and Reconstruction-Inhibited Transition Metal Sulfide Catalysts via Tailoring Electron-Deficient Distribution for Water Oxidation," *ACS Catal* 12 (2022): 13234–13246, https://doi.org/10.1021/acscatal.2c03338.

75. Y. Wu, X. Tao, Y. Qing, et al., "Cr-Doped FeNi–P Nanoparticles Encapsulated into N-Doped Carbon Nanotube as a Robust Bifunctional Catalyst for Efficient Overall Water Splitting," *Advanced Materials* 31 (2019): 1900178, https://doi.org/10.1002/adma.201900178.

76. J. Huang, J. Chen, T. Yao, et al., "CoOOH Nanosheets With High Mass Activity for Water Oxidation," *Angewandte Chemie International Edition* 54 (2015): 8722–8727, https://doi.org/10.1002/anie.201502836.

77. Y. Wang, J. Wang, J. Xu, et al., "Fullerene-Buffered Electron Shuttle of Ru/RuO_2 With Switchable Active Sites Enables Robust and Efficient Bifunctional Alkaline Water Electrolysis," *Angewandte Chemie International Edition* 64 (2025): e202503608, https://doi.org/10.1002/anie.202503608.

Supporting Information

Additional supporting information can be found online in the Supporting Information section.

Supporting File: anie72237-sup-0001-SuppMat.docx.

15213773, 2026, 23, Downloaded from https://onlinelibrary.wiley.com/doi/10.1002/anie.9878440 by Xinlin Yang - South University Of Science , Wiley Online Library on [02/06/2026]. See the Terms and Conditions (https://onlinelibrary.wiley.com/terms-and-conditions) on Wiley Online Library for rules of use; OA articles are governed by the applicable Creative Commons License